Summertime Coupling between Sea Surface Temperature and Wind Stress in the California Current System

DUDLEY B. CHELTON

College of Oceanic and Atmospheric Sciences, and Cooperative Institute for Oceanographic Satellite Studies, Oregon State University, Corvallis, Oregon

MICHAEL G. SCHLAX

College of Oceanic and Atmospheric Sciences, Oregon State University, Corvallis, Oregon

ROGER M. SAMELSON

College of Oceanic and Atmospheric Sciences, and Cooperative Institute for Oceanographic Satellite Studies, Oregon State University, Corvallis, Oregon

(Manuscript received 28 December 2005, in final form 22 June 2006)

ABSTRACT

Satellite observations of wind stress and sea surface temperature (SST) are analyzed to investigate ocean–atmosphere interaction in the California Current System (CCS). As in regions of strong SST fronts elsewhere in the World Ocean, SST in the CCS region is positively correlated with surface wind stress when SST fronts are strong, which occurs during the summertime in the CCS region. This ocean influence on the atmosphere is apparently due to SST modification of stability and mixing in the atmospheric boundary layer and is most clearly manifest in the derivative wind stress fields: wind stress curl and divergence are linearly related to, respectively, the crosswind and downwind components of the local SST gradient. The dynamic range of the Ekman upwelling velocities associated with the summertime SST-induced perturbations of the wind stress curl is larger than that of the upwelling velocities associated with the mean summertime wind stress curl. This suggests significant feedback effects on the ocean, which likely modify the SST distribution that perturbed the wind stress curl field. The atmosphere and ocean off the west coast of North America must therefore be considered a fully coupled system. It is shown that the observed summertime ocean–atmosphere interaction is poorly represented in the NOAA North American Mesoscale Model (formerly called the Eta Model). This is due, at least in part, to the poor resolution and accuracy of the SST boundary condition used in the model. The sparse distribution of meteorological observations available over the CCS for data assimilation may also contribute to the poor model performance.

1. Introduction

The structure of the wind field is poorly known over the California Current System (CCS), which extends at least 500 km offshore from the west coast of the United States. Historical observations from ships and buoys in this region are mostly restricted to a band within about 150 km of the coast (Figs. 1 and 2). The winds over the CCS have been modeled with ~10 km grid resolution by several mesoscale atmospheric models, but the quality of these model wind fields has been difficult to assess except near coastal wind gauges, coastal wind profilers, and buoys (e.g., Koračin and Dorman 2001; Pickett et al. 2003). Knowledge of the wind field is worse in other eastern boundary current regions where in situ observations are even sparser. Satellite radar scatterometers provide the only comprehensive high-resolution observations of the vector wind field throughout the World Ocean. The objective of this study is to investigate the structure of the wind stress field over the CCS from measurements by the SeaWinds scatterometer on the National Aeronautics and Space Administration (NASA) Quick Scatterometer

Corresponding author address: Dudley B. Chelton, College of Oceanic and Atmospheric Sciences, 104 COAS Administration Building, Oregon State University, Corvallis, OR 97331-5503.
E-mail: chelton@coas.oregonstate.edu

DOI: 10.1175/JPO3025.1

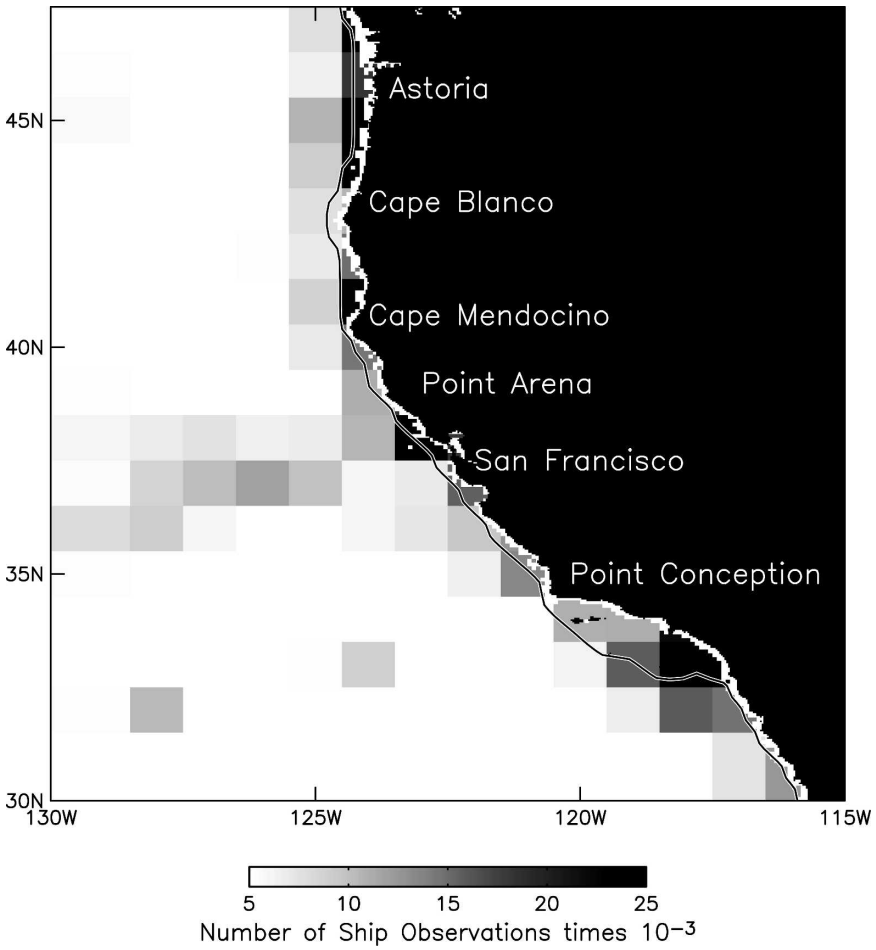

FIG. 1. The geographical distribution of ship observations in 1° latitude by 1° longitude regions in the Comprehensive Ocean–Atmosphere Data Set (COADS; Woodruff et al. 1987) over the 38-yr period 1960–97. The white areas correspond to 1° squares with fewer than about one observation per three days, on average. Areas with the darkest gray shade correspond to 1° squares with an average of more than about two observations per day over the 38-yr time period. Some of these cells contain as many as 2 times this many observations, most notably the 1° squares nearest the mouths of San Francisco Bay and Long Beach Harbor in southern California. The line running approximately parallel to the coast represents the ~30 km extent of land contamination in the 25-km QuikSCAT measurements of wind stress.

(QuikSCAT) satellite. The emphasis is on the summertime upwelling season, defined here to be June through September.

Some of the conclusions of this study can be anticipated from recent analyses of QuikSCAT data in other regions. As reviewed by Xie (2004) and Chelton et al. (2004), QuikSCAT data have revealed that sea surface temperature (SST) exerts a remarkably strong influence on the wind stress field throughout the World Ocean wherever there are strong SST fronts. This ocean–atmosphere interaction apparently arises from SST modification of stability and vertical mixing in the atmospheric boundary layer. Based on earlier in situ observations in the Gulf Stream, Agulhas Current, and eastern tropical Pacific regions, respectively, Sweet et al. (1981), Jury and Walker (1988), and Wallace et al. (1989) hypothesized that enhanced vertical turbulent mixing as cold air passes over warm water deepens the boundary layer and mixes momentum downward from aloft to the sea surface, thus accelerating the surface winds. The modeling study by de Szoeke and Bretherton (2004) of winds blowing from cold to warm water across the SST front on the north side of the Pacific equatorial cold tongue supports this interpretation of the observations.

Several aspects of the coupling are not yet understood. Samelson et al. (2006) argue that the "downward mixing" mechanism cannot explain the observed decel-

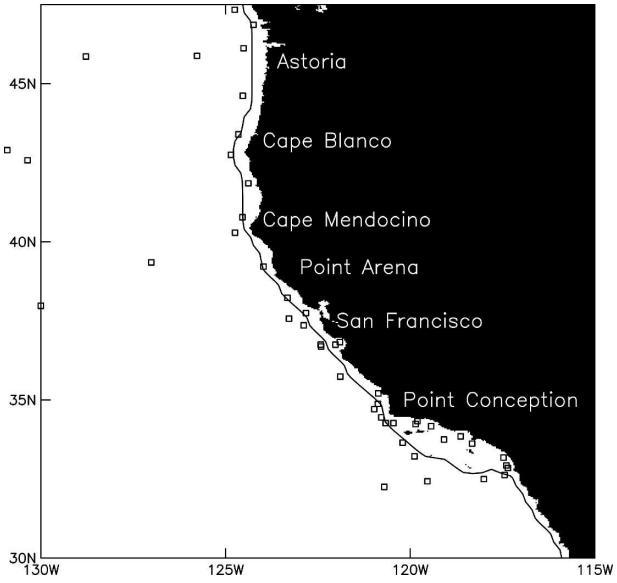

FIG. 2. The locations of buoys with wind anemometers off the west coast of North America (see online at http://www.ndbc.noaa.gov). As in Fig. 1, the line running approximately parallel to the coast represents the ~30 km extent of land contamination in the 25-km QuikSCAT measurements of wind stress.

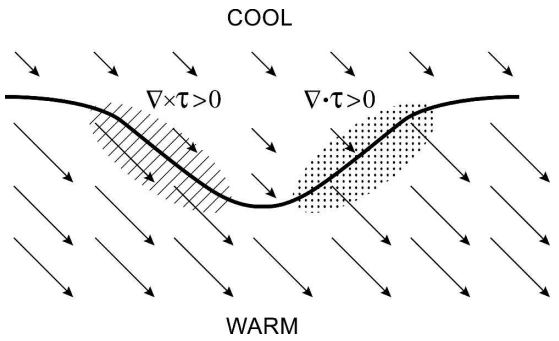

FIG. 3. Schematic summary of the influence of SST on winds near a meandering SST front. The wind stress magnitudes (represented by the lengths of the vectors) are relatively strong over warm water and weak over cold water, which generates local curl and divergence of the wind stress. The curl is strongest where the winds blow parallel to isotherms (hatched region) and the divergence is strongest where winds blow perpendicular to isotherms (stippled region). The wind stress curl and divergence are therefore linearly related to the local crosswind and downwind components of the SST gradient, respectively (see Fig. 7).

eration of surface winds over cold water, and suggest an alternative, quasi-equilibrium, model that offers a possible explanation for both the warm acceleration and the cold deceleration. In this model, the stress vanishes at the top of the atmospheric boundary layer and the vertical divergence of the stress in the boundary layer is approximately constant. This implies that the surface wind stress is linearly related to the atmospheric boundary layer thickness. Surface winds are therefore weaker over cold water where the boundary layer thins due to decreased vertical mixing. Small et al. (2005) suggest that secondary circulations driven by SST-induced pressure gradients may also play a role. The atmospheric boundary layer processes responsible for the observed coupling between SST and surface winds are thus the subject of ongoing research.

Regardless of the detailed dynamics and thermodynamics of the SST influence on the atmospheric boundary layer, the observed ocean–atmosphere interaction in the vicinity of meandering SST fronts such as those found in the CCS during the summertime (Strub and James 2000; Castelao et al. 2006) induces curl and divergence in the wind stress field. As shown schematically in Fig. 3 and discussed by Chelton et al. (2001, 2004), O'Neill et al. (2003, 2005), and Maloney and Chelton (2006) for a variety of regions of the World Ocean, locally high wind stress over warm water and low wind stress over cold water generate a curl that varies linearly with the crosswind component of the SST gradient and a divergence that varies linearly with the downwind component of the SST gradient.

The wind stress curl is of particular interest oceanographically as it generates open ocean upwelling and downwelling through Ekman pumping (Gill 1982; Cushman-Roisin 1994). Pickett and Paduan (2003) have argued from mesoscale model wind fields that curl-driven Ekman upwelling is comparable to coastal upwelling along the California and Oregon coasts. When spatially integrated, the volume transport of the curl-driven upwelling velocity was about double the Ekman transport from coastal upwelling. Dever et al. (2006) obtained similar results based on analysis of direct observations of wind stress and wind stress curl over the inner 25 km of the California shelf at about 38°N. The vertical velocity from coastal upwelling was 3 to 5 times greater than that from curl-driven Ekman upwelling over the nearshore region. However, the spatially integrated upwelling volume transport from the wind stress curl was about twice that from coastal upwelling because of the larger area over which the curl-driven upwelling occurred. From analysis of QuikSCAT winds off Oregon and northern California, Huyer et al. (2005) similarly found that the coastal upwelling velocity was an order of magnitude stronger than the curl-driven upwelling velocity, but that the integrated volume transport from curl-driven upwelling was comparable to the Ekman transport from coastal upwelling.

The open-ocean studies of SST influence on surface winds that have been conducted to date in other regions have been based primarily on simultaneous measure-

ments of wind stress by QuikSCAT and near-all-weather (nonraining conditions) microwave measurements of SST. In particular, global measurements of SST from the Advanced Microwave Scanning Radiometer on the Earth Observing System (EOS) *Aqua* satellite (AMSR-E) have allowed investigation of SST influence on surface winds in midlatitude regions of strong SST fronts associated with midlatitude jets such as the Gulf Stream, Kuroshio Extension, Agulhas Return Current, and Antarctic Circumpolar Current (Chelton et al. 2004; O'Neill et al. 2005; Maloney and Chelton 2006). The present study utilizes these AMSR-E data and is therefore limited primarily to the time period since June 2002 when the AMSR-E data record began. (Six years of QuikSCAT data from August 1999 through September 2005 are considered in section 6.)

The QuikSCAT and AMSR-E datasets are summarized in section 2. SST influence on the wind stress field over the CCS is investigated in sections 3 and 4 for the time period June 2002–September 2005, which corresponds to the first 40 months of the AMSR-E data record. The ability of high-resolution atmospheric models to represent the observed SST influence on surface winds is investigated in section 5 from the National Oceanic and Atmospheric Administration (NOAA) North American Mesoscale (NAM) Model (formerly called the Eta Model). Implications of the results of this study are discussed in section 6 and the conclusions are summarized in section 7.

2. Data description

a. QuikSCAT measurements of surface wind stress

As summarized in detail by Chelton and Freilich (2005), scatterometers infer the surface wind stress magnitude from radar backscatter, which increases with increasing wind-induced roughness of the sea surface. For a given wind stress, the backscatter varies with the antenna pointing angle relative to the wind direction. Wind direction is thus obtained from measurements at multiple antenna angles that are acquired from fore and aft views of a given location on the sea surface as the satellite moves along in its orbit.

For convenience for a wide range of applications, scatterometer measurements of the wind stress are reported as the equivalent neutral-stability wind at 10-m height above the sea surface (i.e., the wind that would exist for a given surface stress if the atmosphere were neutrally stable). The equivalent neutral stability 10-m wind speed is typically a few tenths of a meter per second higher than the actual 10-m wind speed and rarely differs from the actual 10-m wind speed by more than 1.5 m s^{-1} (Mears et al. 2001). Surface stresses are obtained from the 10-m winds using a neutral-stability drag coefficient, regardless of the actual atmospheric stability at the time of the measurement. The drag coefficient used here is the modified Large–Pond drag coefficient for neutrally stable conditions (see the appendix of Large et al. 1994).

The accuracy of scatterometer wind retrievals is best characterized in terms of vector component errors (Freilich and Dunbar 1999). When compared with high-quality buoy winds corrected for atmospheric stability effects (i.e., converted to 10-m equivalent neutral-stability winds), the accuracy of the QuikSCAT winds analyzed here is about 0.75 m s^{-1} in the along-wind component and about 1.5 m s^{-1} in the crosswind component (Chelton and Freilich 2005). Wind direction accuracy is thus a sensitive function of wind speed at low wind speeds but improves rapidly with increasing wind speed. At wind speeds higher than about 6 m s^{-1}, the QuikSCAT directional accuracy is about 14°. Assuming that the component errors are uncorrelated, the overall accuracy of scatterometer estimates of equivalent neutral-stability 10-m wind speed is about 1.7 m s^{-1}. The accuracies of scatterometer measurements of equivalent neutral-stability 10-m wind speed and direction are thus comparable to those of measurements from a well-calibrated buoy (Stoffelen 1998; Freilich and Dunbar 1999).

The accuracies of QuikSCAT wind retrievals are degraded when rain significantly contaminates the radar footprint. For the analysis presented here, rain-contaminated observations were flagged and excluded from further analysis based on the so-called multidimensional histogram-based (MUDH) algorithm (Huddleston and Stiles 2000; Stiles and Yueh 2002).

On each orbital pass, QuikSCAT measurements are available across a swath width of about 1600 km. This results in more than 90% coverage of the CCS region each day (Schlax et al. 2001). Measurements from descending and ascending ground tracks occur in the CCS region at approximately 0300 and 1400 UTC, respectively, which correspond to summertime local times of 2000 and 0700 PDT. In the standard processing of QuikSCAT data,[1] the footprint size is about 25 km and

[1] With special processing, a footprint size of about 12.5 km can be obtained and it may be possible to measure winds closer than 30 km to the coast. At present, however, these higher-resolution QuikSCAT wind retrievals are experimental (M. H. Freilich 2005, personal communication). The analysis here is based on the 25-km QuikSCAT winds obtained from the standard processing.

measurements closer than about 30 km to land (Figs. 1 and 2) are contaminated by radar backscatter from land in the antenna side lobes.

The QuikSCAT data record began in July 1999. Over the June 2002–September 2005 time period considered in sections 3 and 4 (the first 40 months of the AMSR-E data record, see section 2b), the typical number of QuikSCAT observations in 0.25° regions was about 1850. The 25-km QuikSCAT wind stresses were smoothed a small amount on a swath-by-swath basis using a loess smoother (Schlax et al. 2001) with a half-power filter cutoff at a wavelength of about 75 km. This is analogous to block averaging over approximately 45-km regions, but the sidelobes of the filter transfer function of the loess smoother are much smaller than those of block averages (see Fig. 1 of Chelton and Schlax 2003). The smoothed stresses from each measurement swath were vector averaged onto the 0.25° latitude by 0.25° longitude grid for the various averaging periods considered in this study. For the "monthly" analyses in section 3, which are the primary focus of this investigation of ocean–atmosphere interaction, the averages consisted of overlapping 29-day means at 7-day intervals.

Because of the complicated space–time sampling pattern of the QuikSCAT observations (Schlax et al. 2001), the operations of averaging and differentiation are noncommutative. The wind stress curl and divergence were therefore computed within each measurement swath from centered differences of the smoothed stress components and averaged temporally on the 0.25° grid in the same manner as the wind stresses. This preserves the signals of each meteorological event observed by QuikSCAT and avoids introducing artifacts from differencing between grid points composed of averages of wind stress vectors over different sets of observation times.

b. AMSR-E measurements of SST

The AMSR-E is one of several instruments on board the EOS *Aqua* satellite. The AMSR-E data record began in June 2002 with 89% global coverage each day. As summarized by Chelton and Wentz (2005), SST retrievals are obtained from measurements of both horizontally and vertically polarized radiance at frequencies of 6.9, 10.7, 18.7, 23.8, and 36.5 GHz. Rain-contaminated AMSR-E measurements of SST are identified and excluded from further analysis using the measurements at 36.5 GHz. The footprint size for SST is about 56 km and the accuracy is about 0.4°C (Chelton and Wentz 2005). Sidelobe contamination at 6.9 GHz with the AMSR-E antenna extends about 75 km from land.

The utility of AMSR-E SST fields in the CCS is limited by the coarse 56-km resolution of the measurements and the 75-km land mask. These limitations are offset by the advantages of near all-weather measurement capability. The more traditional infrared measurements with 1-km resolution from the Advanced Very High Resolution Radiometer (AVHRR) on the operational NOAA polar-orbiting satellites can only be obtained in clear-sky conditions. In the CCS region, this typically restricts the AVHRR coverage to about 50%, which can be compared with the AMSR-E coverage of about 95% (see Figs. 1 and 3 of Chelton and Wentz 2005). During the June–September summertime period that is of primary interest in this study, the AVHRR coverage is often limited to less than 30% because of low-level stratus clouds that form over the cold upwelled water found within a few hundred kilometers of the coast. The AMSR-E data clearly show the SST influence on surface winds in the CCS (see sections 3 and 4), despite the limitations of the 56-km resolution and 75-km land mask.

The SST measurements from each overpass during the first 40 months of the version-5 AMSR-E dataset (more information was available online at www.remss.com) were bilinearly interpolated to the same 0.25° latitude by 0.25° longitude grid as the QuikSCAT measurements of wind stress, curl, and divergence and were then bin averaged in overlapping 3-day periods at daily intervals. For the analysis in sections 3 and 4, the downwind and crosswind components of the SST gradients were computed within each QuikSCAT measurement swath from the instantaneous in-swath QuikSCAT smoothed wind stress described in section 2a and the 3-day average AMSR-E SST field centered on the date of the QuikSCAT swath.[2] For the monthly analysis in section 3, these SST gradient components were averaged temporally in the same manner as the wind stress fields as described in section 2a.

3. SST influence on the surface wind stress field

Environmental conditions in the CCS are fundamentally different during summertime and wintertime. The statistics computed from the daily-average QuikSCAT

[2] This procedure differs from that used in our previous air–sea interaction studies (Chelton et al. 2001, 2004; O'Neill et al. 2003, 2005; Chelton 2005) in which SST gradient components were computed from time-averaged stress and SST fields. Because the downwind and crosswind components of the SST gradient are nonlinear quantities, the procedure used here is the correct one. Comparisons with our previous results determined that the differences were relatively small and did not significantly change any of our past conclusions.

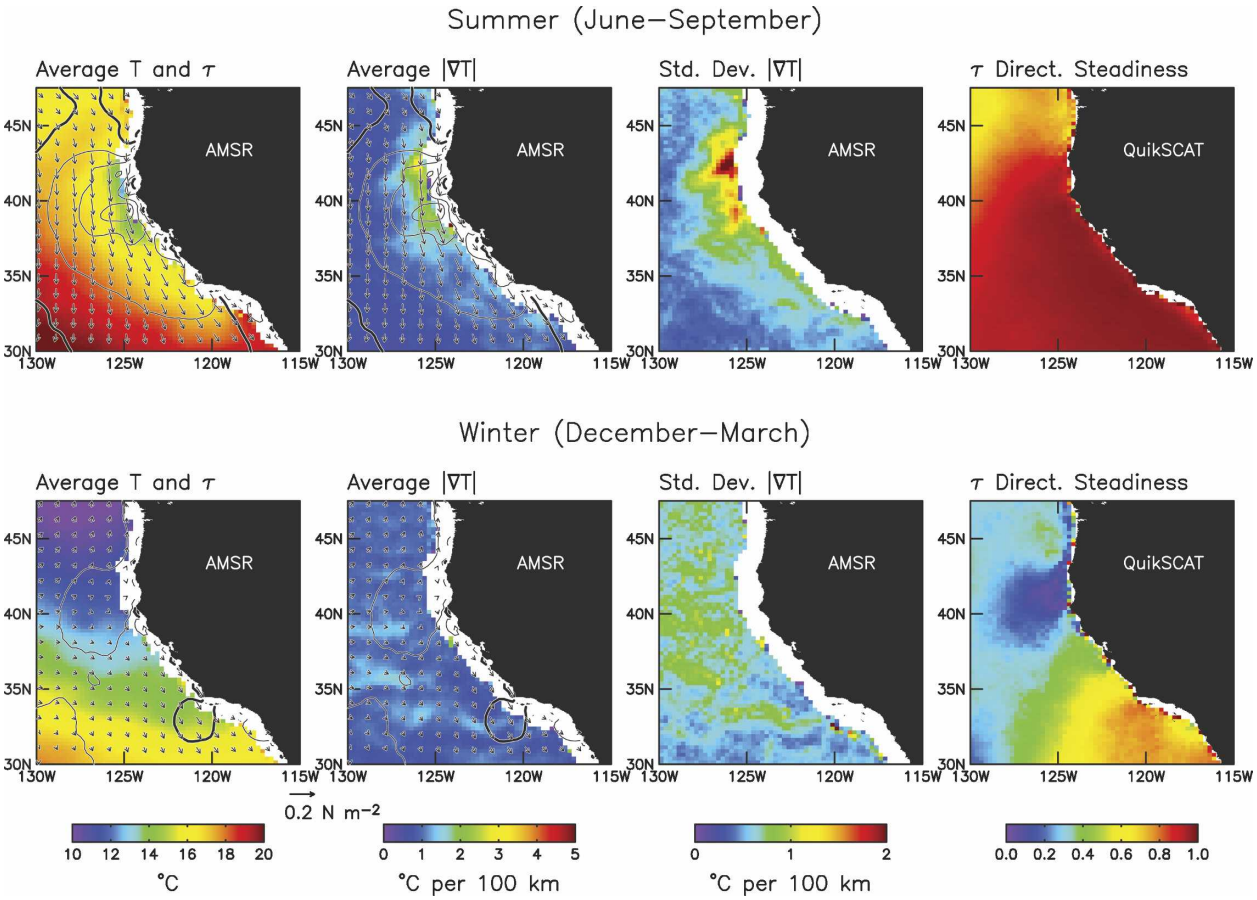

FIG. 4. (top) Summertime (Jun–Sep) and (bottom) wintertime (Dec–Mar) statistics of SST and wind stress fields computed from daily averages of AMSR-E and QuikSCAT data during the 40-month period June 2002–September 2005: (left to right) Average SST with vector-average wind stress overlaid; average SST gradient magnitude with vector-average wind stress overlaid; standard deviation of SST gradient magnitude; and wind stress directional steadiness, defined to be the magnitude of the vector-average wind stress divided by the scalar average of the wind stress magnitude computed from daily-averaged QuikSCAT data in the respective seasons. In the left four panels, the 0.25° gridded vector-average QuikSCAT wind stress vectors are displayed on a coarse 1° × 1° grid for clarity, the contours are the magnitude of the vector-average wind stress with a contour interval of 0.03 N m^{-2}, and the heavy contour corresponds to 0.06 N m^{-2}.

data in the top panels in Fig. 4 show that summertime wind stress is characterized by very steady equatorward alongshore directions[3] (directional steadiness greater than 0.9) everywhere south of about 43°N (right panel). The directional steadiness decreases somewhat to about 0.75 north of 43°N. In association with the persistently upwelling-favorable equatorward summertime winds, there is a nearshore band of cold water that extends offshore more than 150 km in the mean (left panel) and is particularly well developed in the region between about 43° and 37°N. The magnitude of the vector-average SST gradient (second panel) is strong within the same region of cold water (see also Castelao et al. 2006). Summertime temporal variability of the SST gradient magnitude (third panel) extends farther offshore in two broad "tongues" that appear to originate at Cape Blanco and Cape Mendocino, though this cannot be confirmed from the AMSR-E data because of the inability to determine SST closer than 75 km to land.

Wintertime conditions (bottom panels in Fig. 4) are characterized by monotonically decreasing SST with increasing latitude. The mean SST gradient field is weak (see also Castelao et al. 2006) and temporal variability of SST gradients within the winter season is only mod-

[3] While the summertime wind direction over the CCS is very steady, it should be noted that the wind stress magnitude varies considerably (see Fig. 14 below). For daily averages of the alongshore component of the wind stress, for example, the summertime temporal autocorrelation function ensemble averaged over the CCS region decreases to a value of about 0.5 at a lag of 1 month.

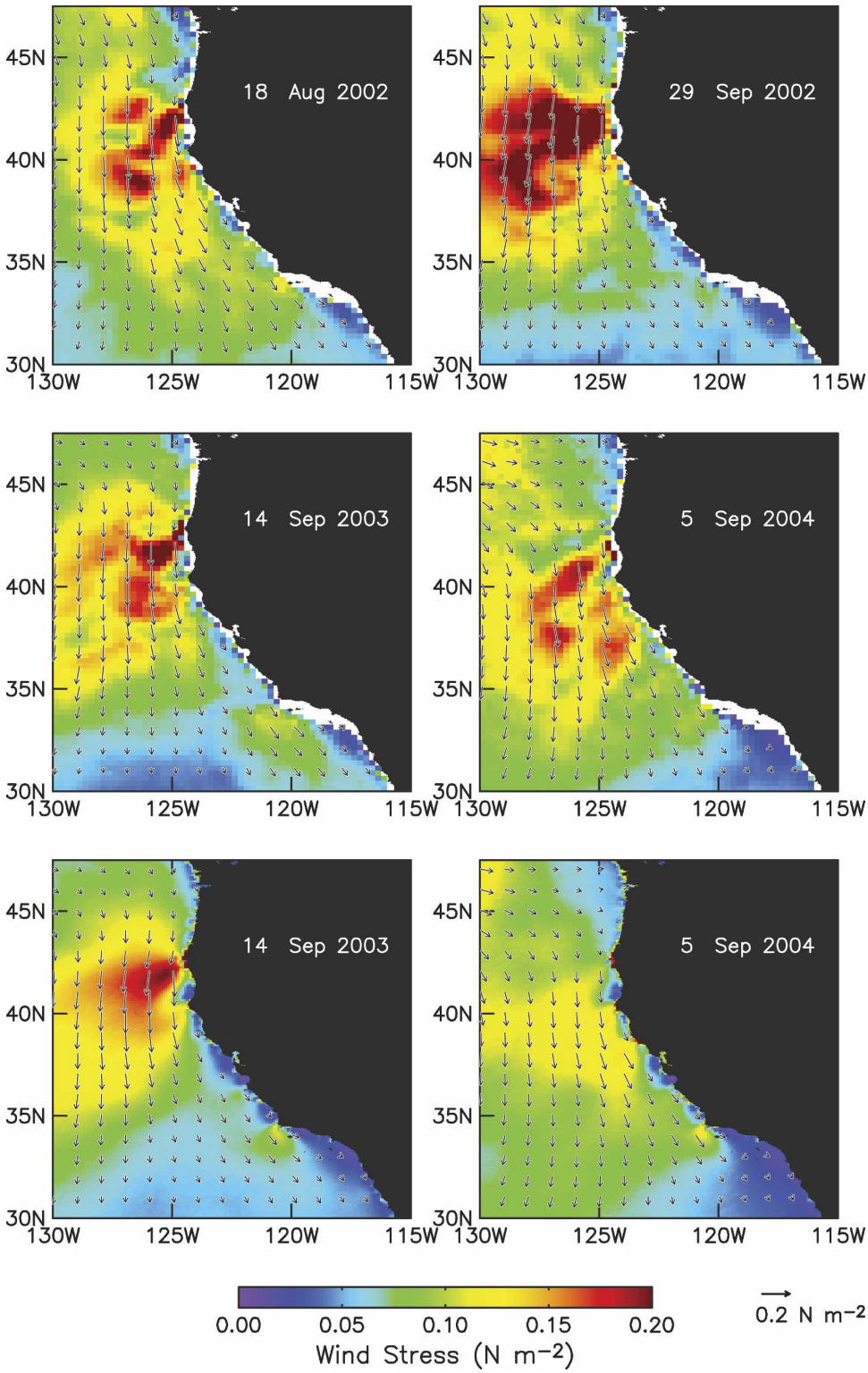

FIG. 5. Example 29-day averages of wind stress over the CCS: (top and middle) 29-day averages of QuikSCAT data centered on 18 Aug 2002, 29 Sep 2002, 14 Sep 2003, and 5 Sep 2004; (bottom) 29-day averages of wind stress from the NAM Model (see section 5) for the same dates as the QuikSCAT wind stress fields in the middle panels. The 0.25° gridded QuikSCAT wind stress vectors and the 12-km NAM wind stress vectors are plotted on a coarse 1° grid for clarity and the color represents the magnitude of the 29-day vector average.

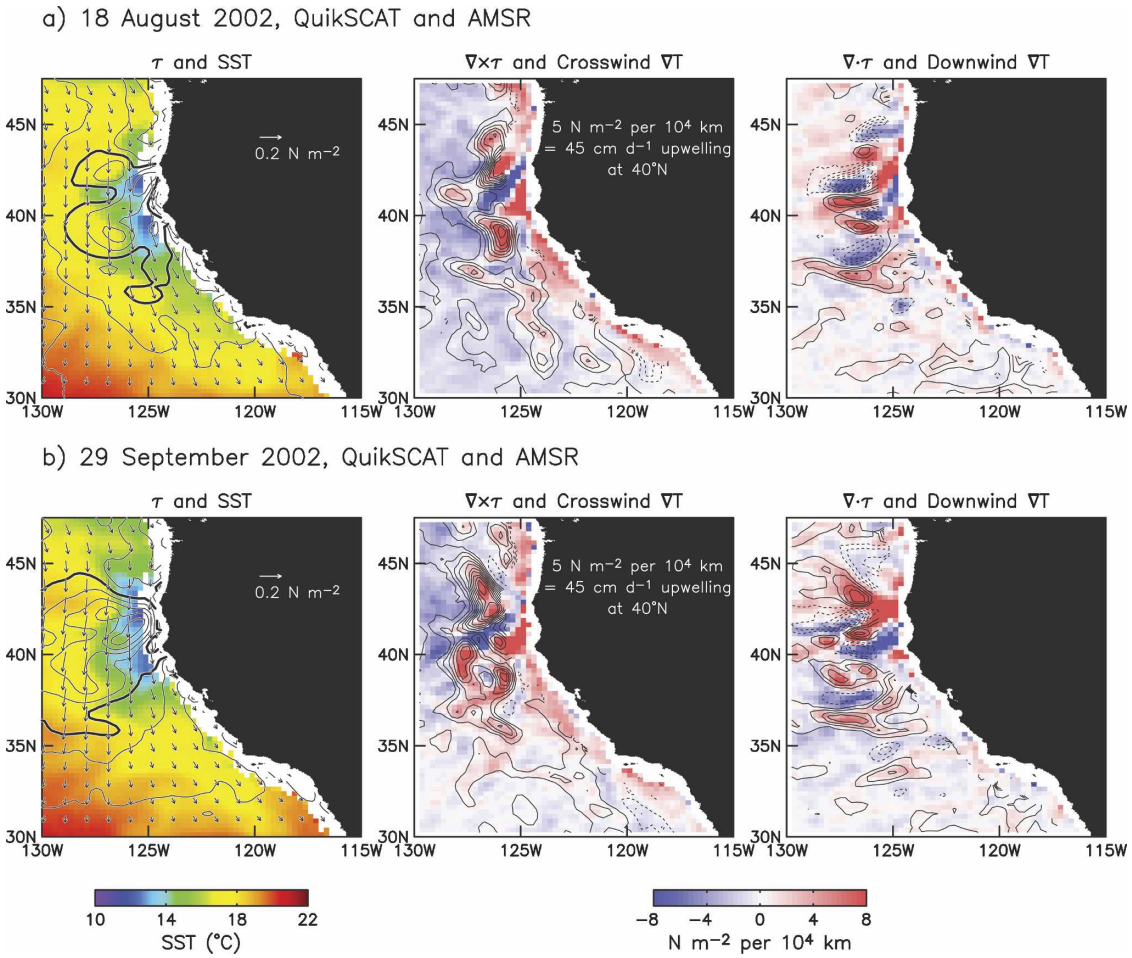

FIG. 6. SST and wind stress fields for the four example 29-day averages of QuikSCAT wind stress shown in the top and middle panels of Fig. 5: (left) AMSR-E estimates of SST with wind stress vectors overlaid, (middle) wind stress curl with contours of crosswind SST gradient, and (right) wind stress divergence with contours of downwind SST gradient. In the left panels, the 0.25° gridded QuikSCAT wind stress vectors are plotted on a coarse 1° × 1° grid for clarity, the contours are the magnitude of the vector-average wind stress with a contour interval of 0.03 N m^{-2}, and the heavy contour corresponds to 0.12 N m^{-2}. The contour interval for the SST gradient components in the middle and right panels is 0.5°C $(100\ km)^{-1}$.

erate. Except in the southeast corner of the region considered here, the wintertime wind stress directional steadiness is low, especially between about 38° and 43°N. Vector-average wintertime winds are weak everywhere, with downwelling-favorable poleward mean winds north of about 43°N and upwelling-favorable equatorward mean winds south of about 40°N. The generally weak vector-average wintertime wind stress is perhaps counterintuitive, especially off northern California and Oregon. While the wind stress associated with individual wintertime storms is high, the large variability in wind direction (low directional steadiness) as synoptic weather systems pass over the CCS results in small vector-average wind stresses in the wintertime mean.

The steady wind direction and strong SST gradients during summertime are favorable for a strong influence of SST on the wind stress. In contrast, the weak SST gradients and low directional steadiness of the wind stress during wintertime combine to create unfavorable conditions for SST influence on the wind stress (see Fig. 9 below). The focus of this study is on the summertime when the ocean–atmosphere interaction is most clearly developed.

The summertime influence of SST on the wind stress is illustrated here from the examples of 29-day averages in the top four panels in Fig. 5 (two from the summer upwelling season of 2002, and one each from the summer upwelling seasons of 2003 and 2004). All four cases correspond to fully developed upwelling conditions

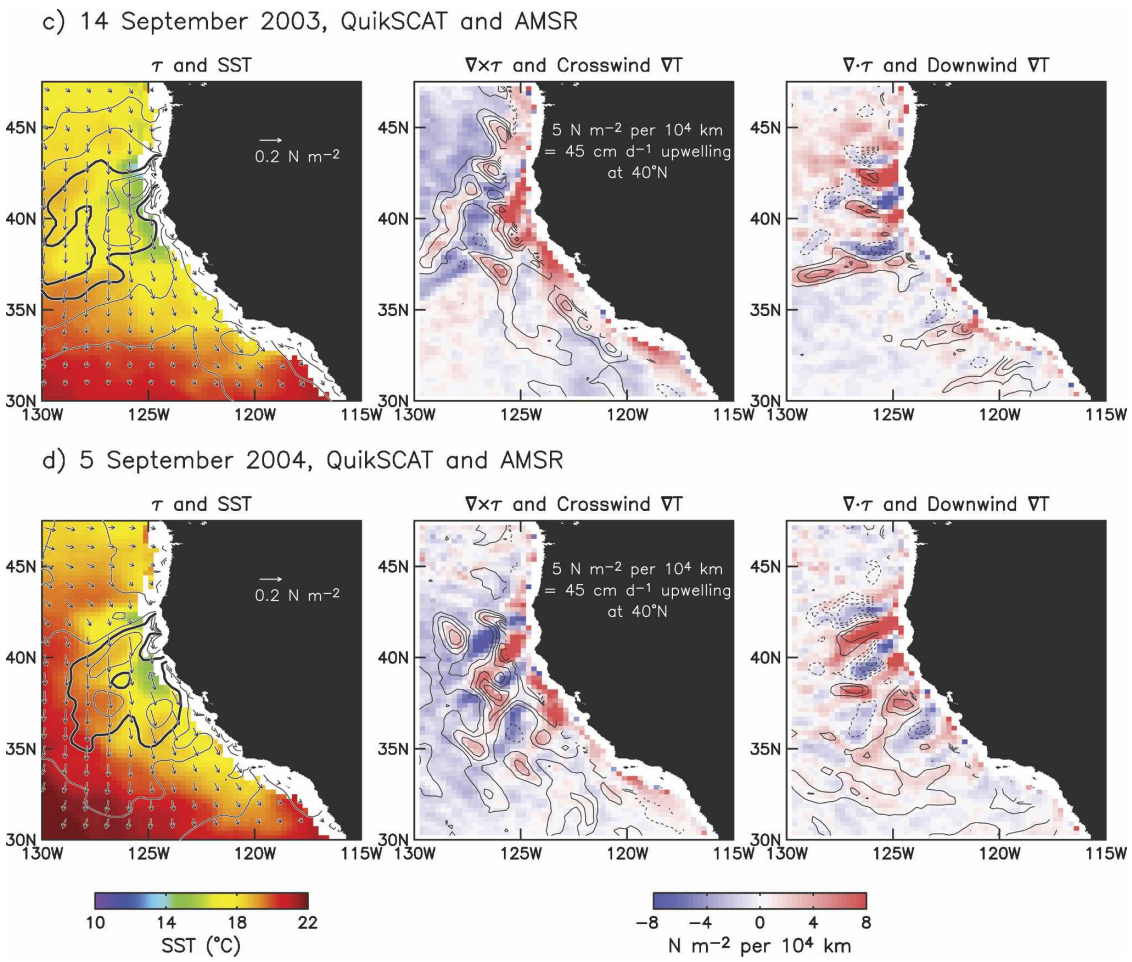

FIG. 6. (*Continued*)

with strong equatorward wind stress off northern California and Oregon. The wind stress is locally intensified over regions extending several hundred kilometers to the southwest of Cape Blanco and Cape Mendocino. The broad offshore extent of the strong winds has previously been noted to the southwest of Cape Mendocino by Dorman et al. (2000) and Edwards et al. (2002) from satellite estimates of wind speed by the Special Sensor Microwave Imager (SSM/I) during the summers of 1994 and 1996.

The small-scale structures in the wind stress fields in the four examples in Fig. 5 are attributable mostly to the influence of SST. This becomes clear from the curl and divergence fields[4] in the middle and right panels in Figs. 6a–d. In all four examples, the spatial pattern of the curl field is visually well correlated with the crosswind component of the SST gradient that is overlaid as contours in the middle panels. Likewise, the spatial pattern of the divergence field is visually well correlated with the downwind component of the SST gradient overlaid as contours in the right panels.

The relations between the 29-day-average derivative wind stress fields (curl and divergence) and their associated components of the SST gradient field are quantified in Fig. 7. As suggested from the schematic description in Fig. 3, the summertime wind stress curl and divergence are approximately linearly related, respectively, to the crosswind and downwind components of the SST gradient field. The binned scatterplot for the curl in the top-left panel in Fig. 7 does not pass through the origin (i.e., zero values on both the abscissa and ordinate) because of the background large-scale mean SST field in which summertime SST increases mono-

[4] Since wind direction cannot be determined from the SSM/I data, it was not possible to compute the curl and divergence fields in the earlier SSM/I-based studies by Dorman et al. (2000) and Edwards et al. (2002).

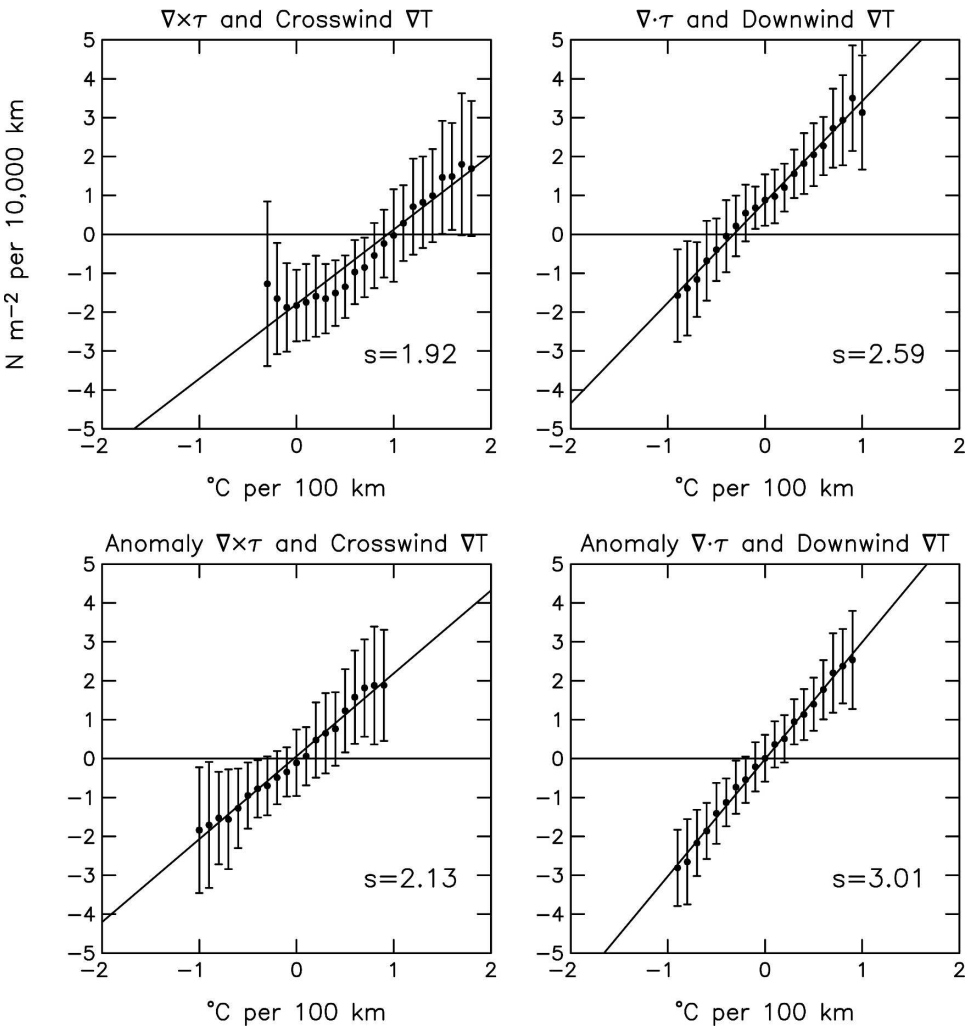

FIG. 7. Binned scatterplots of (left) summertime wind stress curl vs the crosswind component of the SST gradient and (right) summertime wind stress divergence vs the downwind component of the SST gradient. (top) The total fields and (bottom) the anomaly fields, defined to be the deviation of each summertime 29-day average from the overall summertime average. The statistics were computed over the region 35°–45°N, 128°–120°W (see the boxes in Fig. 8 below). The points in each are the means within each bin computed from overlapping 29-day averages at 7-day intervals in the four June–September time periods during calendar years 2002–05. The error bars in each represent the ±1 standard deviation over all of the individual 29-day averages within each bin. The slope *s* of the least squares fit line to the binned averages is labeled for each.

tonically away from the coast. For the persistently equatorward summertime winds, this superimposes a mean positive crosswind SST gradient on the small-scale SST perturbations that influence the wind stress curl field. When the overall mean summertime curl and crosswind SST gradient fields are removed from each summertime 29-day average, the binned scatterplot for the resulting anomaly curl fields (bottom-left panel in Fig. 7) does pass through the origin and the relationship to the crosswind SST gradient is more linear. The differences in the slopes of the least squares fit lines for the total and anomaly curl and divergence fields are not statistically significant.

A notable characteristic of all four of the examples in Fig. 6 is the triplet of parallel bands of strong positive and negative wind stress curl oriented diagonally southwest from the southern Oregon coast. The lines of zero curl that bracket the band of negative curl in the middle emanate from the coast just north and south of Cape Blanco. These features have been noted from previous analyses of QuikSCAT data by Perlin et al. (2004) and Huyer et al. (2005). In association with these curl bands,

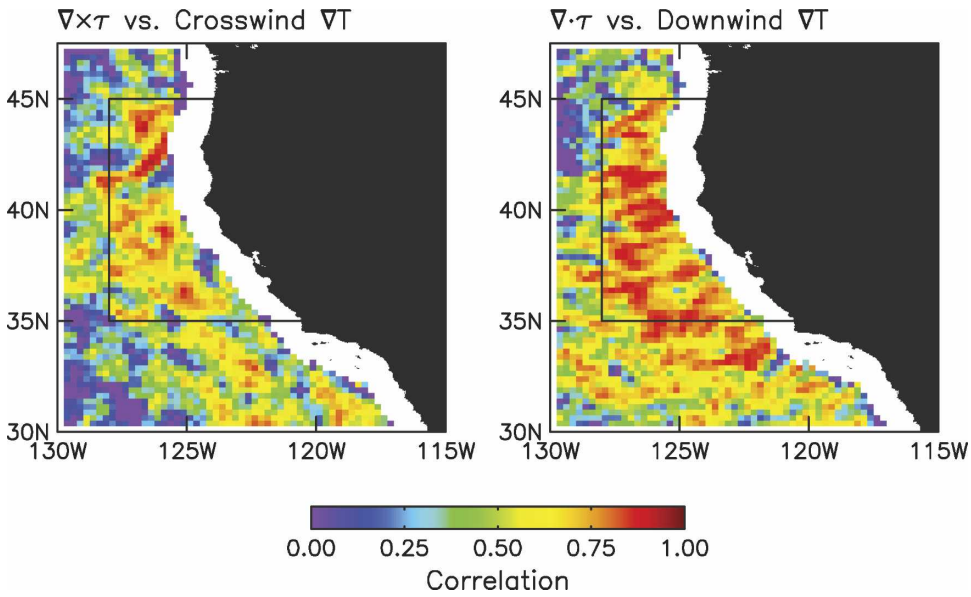

FIG. 8. Maps of the correlations (left) between the wind stress curl and the crosswind SST gradient and (right) between the wind stress divergence and the downwind SST gradient computed from summertime 29-day averages. The box represents the region over which the statistics in Fig. 7 and the time series in Fig. 9 were computed.

there is a triplet of approximately collocated wind stress divergence bands of opposite sign. (The northern band of positive divergence is somewhat less well defined than the other divergence and convergence bands.)

As evidenced by the contours overlaid in Fig. 6, the triplet bands of curl and divergence are associated with the expected structures in the crosswind and downwind SST gradients over most of the region. The one exception is the band of negative wind stress curl that is oriented diagonally southwest from Cape Blanco in all four examples. While the crosswind SST gradient is weak in this band, it does not become negative, as would be expected from Fig. 7. This region of inconsistency between the wind stress curl and the crosswind SST gradient is evident as a region of low cross-correlation in the left panel in Fig. 8. A similar region of low cross-correlation exists directly south of Cape Mendocino near 37°N, 124°W. The association of these two regions of low correlations with Cape Blanco and Cape Mendocino suggests that the orographic influence of these two coastal promontories on the wind stress curl field may extend several hundred kilometers from the capes. The patches of low cross-correlation in the southern CCS region are probably not significant since the crosswind SST gradients are weak in this region. The orographic effects of Cape Blanco and Cape Mendocino apparently have little influence on the divergence field in the offshore regions; the cross-correlation between wind stress divergence and downwind SST gradient is high over most of the CCS region (right panel in Fig. 8).

Nearshore orographic influence of Cape Blanco and Cape Mendocino on the curl and divergence have been discussed from several mesoscale atmospheric modeling studies [see, e.g., Koračin and Dorman (2001) for the divergence, and Pickett and Paduan (2003), Koračin et al. (2004), and Haack et al. (2005) for the curl]. These features in the model wind stress curl and divergence fields are restricted to the very nearshore regions. The 75-km gap in the AMSR-E data near land, which increases to about 100 km in the derivative SST gradient component fields computed from the 0.25° gridded SST fields, limits the ability to determine the relative importance of SST and orographic influence on the wind stress field in these nearshore regions. The SST influence implied by the high correlations of the curl and divergence with their associated SST gradient components beyond 100 km from the coast presumably also influences the structures of the curl and divergence fields closer inshore.

The broad offshore extent of the region of high winds off northern California evident in all four examples of QuikSCAT wind stress fields in Fig. 5 has been discussed extensively by Edwards et al. (2002) who argue that this is a manifestation of supercritical flow in which the wind speeds are faster than the baroclinic gravity wave speed. They interpret the strongest winds downwind of Cape Mendocino as an expansion fan that oc-

curs in association with the 28° bend in the California coastline that creates a hydraulic jump in the supercritical flow, a downstream thinning of the atmospheric boundary layer, and a pressure acceleration of the winds. It is well established from observations and models that such expansion fans develop downwind of major capes along the California coast (e.g., Dorman 1985; Winant et al. 1988; Samelson 1992; Samelson and Lentz 1994; Enriquez and Friehe 1995; Burk and Thompson 1996; Dorman et al. 1999; Burk et al. 1999; Rogerson 1999; Haack et al. 2001, 2005; Edwards et al. 2001; Samelson et al. 2002).

The regions of strong winds southwest of Cape Blanco and Cape Mendocino may be larger in areal extent than can be explained entirely as expansion fans. The observed structures in the QuikSCAT data are at least partly attributable to the influence of SST as discussed above from the curl and divergence fields. A scenario that could broaden the influence of nearshore expansion fans is that the equatorward wind stress at the coast and nearshore positive wind stress curl associated with an expansion fan could generate upwelling of cold water, as suggested by Enriquez and Friehe (1995) and Samelson et al. (2002). Offshore spreading as a cold-water plume would diminish the equatorward wind stress over the cold plume and then accelerate the winds over the warmer water equatorward of the plume. The net effect of this spatial variability of the wind stress would be to create a band of stronger equatorward wind stress that extends southwestward from a more localized expansion fan near the capes.

Regardless of whether the large offshore extent of the expansion fan could exist without SST influence, it is clear that both effects must be taken into consideration in interpretation of the detailed structure of the wind stress field off northern California and Oregon.

In contrast to its strong summertime influence, the coupling between SST and wind stress that is of interest in this study has little or no influence on the 29-day average wind stress fields during winter. Wintertime maps (not shown here) like the summertime maps shown in Figs. 5 and 6 reveal only occasional isolated pockets of weak correlation between the wind stress curl and the crosswind SST gradient, or between the wind stress divergence and the downwind SST gradient.

The strong seasonality of the influence of SST on the wind stress field in the 29-day averages considered here is shown in the bottom panel in Fig. 9. The correlations of both the curl and the divergence with their associated components of the local SST gradient vector are typically higher than 0.5 during the summertime (June–September) and decrease to less than 0.25 during the wintertime. These seasonal variations of the correlation are in phase with seasonal variations of the spatial variability of the SST gradient field (top panel). SST thus influences the wind stress only in the summertime when well-developed fronts are present. The strongest correlations of wind stress curl and divergence with the components of the SST gradients also occur after the large-scale wind field (as represented by the dominant EOF of alongshore wind stress in Fig. 10) becomes equatorward (second panel in Fig. 9) with high directional steadiness (third panel in Fig. 9).

The weak wintertime influence of SST on the wind stress curl and divergence is most likely due primarily to the weak magnitudes and lack of organization of the SST gradients in the winter (bottom panels in Fig. 4; see also Castelao et al. 2006). Another possible contributing factor is that SST might not be able to cool sufficiently in the winter to stabilize the atmospheric boundary layer because of the cold wintertime air temperature. Such stabilization may be necessary for SST-induced spatial variability in the wind stress to develop and become apparent in the curl and divergence fields.

The onset and termination of atmospheric conditions favorable to strong summertime ocean–atmosphere interaction occur quickly in the 29-day average fields considered here. As shown in the third panel in Fig. 9, the "spring transition" from stormy wintertime winds with highly variable direction to summertime equatorward winds with high directional steadiness occurred in May 2003, May 2004, and July 2005. The exact timing of the spring transition can apparently vary in some years. The "fall transition" back to low directional steadiness occurred between early and late October of all three fall (autumn) periods analyzed here (2002, 2003, and 2004). It is evident from the bottom panel in Fig. 9 that the strong influence of SST on the wind stress curl and divergence becomes well established within about a month of the spring transition of the wind field and begins to break down shortly after the fall transition.[5]

4. Adjustment time scales

The changes in the patterns of the wind stress, wind stress curl, and wind stress divergence fields between the first two 29-day average examples shown in Figs. 5 and 6, which are separated in time by six weeks, provide a sense of how quickly the SST and wind stress fields evolve over the course of a summer upwelling season.

[5] These spring and fall transitions of atmospheric conditions may be related to the spring and fall transitions that have been documented in the ocean currents off northern California and Oregon (see Huyer et al. 1979; Strub and James 1988; and references therein).

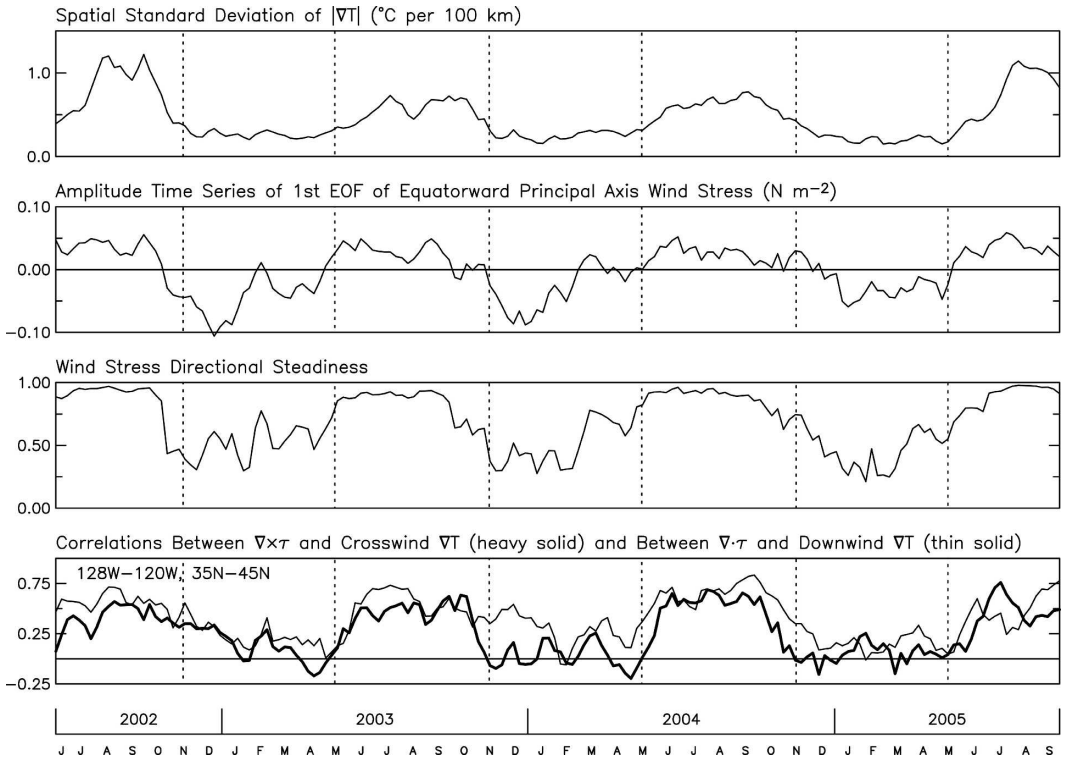

FIG. 9. Time series of statistics computed from AMSR-E and QuikSCAT data in the region 35°–45°N, 128°–120°W (see the boxes in Fig. 8) from overlapping 29-day averages at 7-day intervals: (top to bottom) the spatial standard deviation of the magnitude of the SST gradient field; the amplitude time series of the dominant EOF of alongshore wind stress (see Fig. 10); the wind stress directional steadiness, defined to be the magnitude of the vector-average wind stress divided by the scalar average of the wind stress magnitude computed from the daily-averaged QuikSCAT data in each 29-day period; and the spatial cross correlations between wind stress curl and the crosswind component of the local SST gradient (thick line), and between wind stress divergence and the downwind component of the local SST gradient (thin line). Vertical dotted lines corresponding to the months of May and November of each year are included for reference.

For both curl and divergence, the summertime temporal autocorrelation functions ensemble averaged over the CCS region decrease to a value of about 0.35 at a lag of 1 month in the 29-day average fields. The rich diversity of small-scale structures that can exist in the summertime wind stress field in association with changes in the meandering SST fronts is evident from the distinctly different patterns in the 29-day average maps in Figs. 6c and 6d compared with those in Figs. 6a and 6b.

Quantifying the time scale of the adjustment of the surface wind stress field to changes in SST is difficult since this air–sea interaction is often masked at any particular time by more energetic background variability of the wind field associated with synoptic weather systems. The weather-related variability is suppressed in the 29-day-average wind stress fields considered in section 3. The correlations of shorter time averages of the derivative wind stress fields with their associated SST gradient components are shown as a function of averaging period in Fig. 11. The effects of weather variability become increasingly significant with decreasing averaging period, resulting in decreased correlations for both the wind stress curl and divergence. The reductions in correlations are small down to an averaging period of about two weeks but drop off more steeply for shorter averaging periods. It is not possible to determine from these observational datasets how much of this dropoff in the correlation is attributable to incomplete adjustment of the atmospheric boundary layer to SST influence on atmospheric stability, as opposed to masking by weather-related variability.

Additional insight into the air–sea interaction process that is responsible for the SST influence on the wind stress field can be inferred from the lagged cross-correlations in Fig. 12. For averaging periods longer than about 11 days, there is no evidence of asymmetry in the lagged cross-correlations. For shorter averaging periods, however, the correlations between the wind stress curl and the crosswind SST gradient are higher

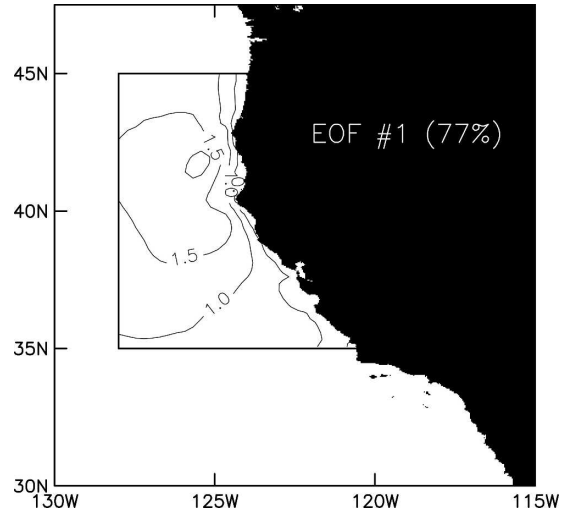

FIG. 10. The dominant EOF of alongshore wind stress computed from overlapping 29-day averages at 7-day intervals over the 40-month time period June 2002–September 2005. The associated EOF amplitude time series is shown in the second panel in Fig. 9. The alongshore direction at each 0.25° grid point was defined to be the angle of the major axis of the wind stress variance ellipse (positive equatorward) computed from summertime daily-averaged QuikSCAT data.

for negative lags than for positive lags, indicating that the wind stress curl perturbations are more highly correlated with earlier perturbations of the crosswind SST gradients than with later perturbations. In contrast, the maximum lagged cross-correlation between the wind stress divergence and the downwind SST gradients occurs at zero lag, even for the shortest averaging period of 1 day. The curl response to crosswind SST gradients is evidently somewhat slower than the divergence response to downwind SST gradients.

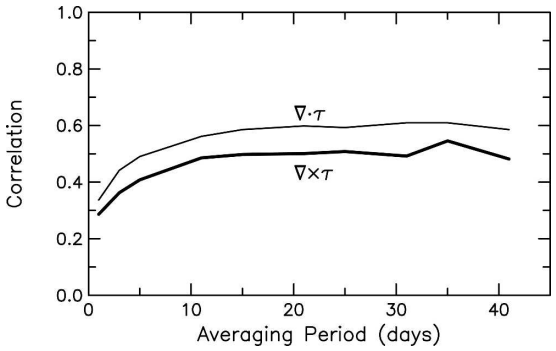

FIG. 11. Correlations between temporal averages of the wind stress curl and the crosswind SST gradient (heavy line) and between temporal averages of the wind stress divergence and the downwind SST gradient (thin line) over the region in the boxes shown in Figs. 8 and 10 as functions of the temporal averaging period in days.

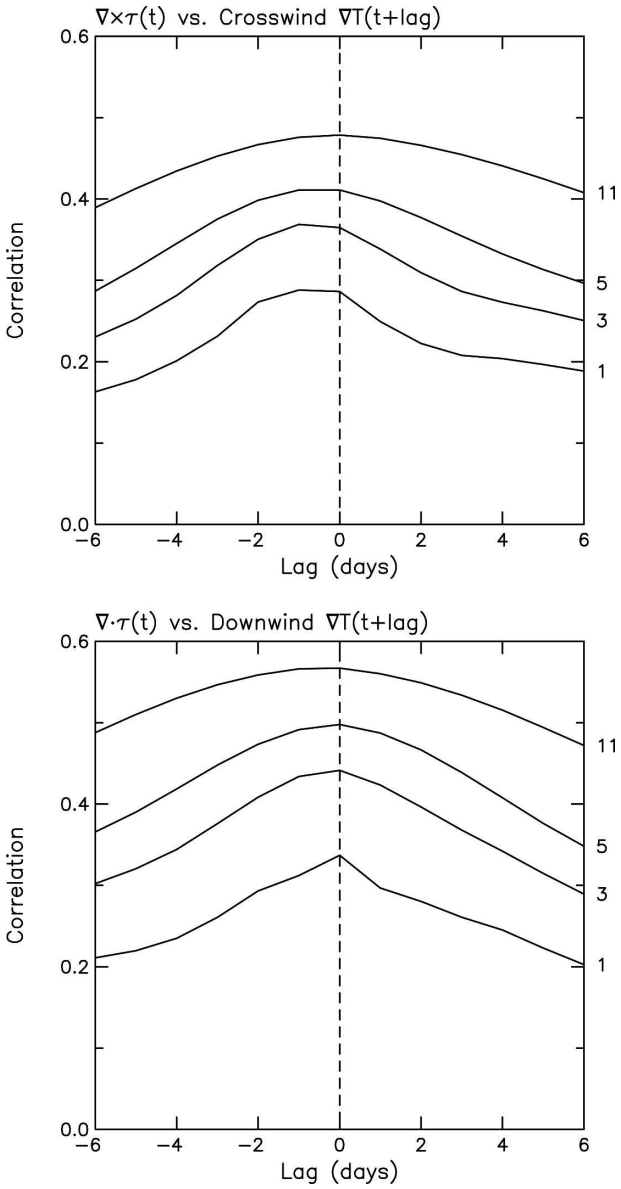

FIG. 12. Lagged correlations (top) between the wind stress curl and the crosswind SST gradient and (bottom) between the wind stress divergence and the downwind SST gradient for temporal averaging periods of 1, 3, 5, and 11 days (bottom to top). Negative lags correspond to the SST gradient component leading the wind stress curl and divergence.

5. Mesoscale model wind stress fields

Atmospheric modeling capabilities have improved to the point where the wind field over the CCS can be modeled with a horizontal resolution of about 10 km (e.g., Dorman et al. 2000; Pickett and Paduan 2003; Koračin et al. 2004; Perlin et al. 2004; Haack et al. 2005). From comparisons with QuikSCAT data, Perlin et al. (2004) concluded that the wind fields from the

operational NOAA Eta Model offered the most accurate of the three mesoscale models that they considered in its representation of the wind field off Oregon. The version of the Eta Model used for that analysis had a grid resolution of 32 km. The resolution was improved to 12 km in 2001 (Rogers et al. 2001) and the model has recently been renamed the NAM Model (Rogers et al. 2005). Summertime NAM wind stress fields are compared here with the QuikSCAT wind stress fields over the three June–September time periods in calendar years 2003–05. Since 30 January 2001, the SST boundary condition in the NAM Model has been the real-time global (RTG) SST fields that are constructed on a 0.5° by 0.5° global grid by objective analysis of ship and buoy observations and infrared satellite observations by the AVHRR (Thiébaux et al. 2003; Chelton and Wentz 2005).

Twice-daily forecast 10-m wind and friction velocity fields at 0300 (3-h forecast) and 1500 UTC (15-h forecast) were used to construct wind stress fields for the analysis presented here.[6] These times coincide closely with the approximate 0300 and 1400 UTC overpass times of QuikSCAT in the CCS region. These twice-daily NAM wind stress fields were bin averaged over the same 0.25° latitude by 0.25° longitude by 29-day periods as the QuikSCAT and AMSR-E data.

Examples of 29-day-average NAM wind stress fields are shown in the bottom two panels in Fig. 5. While the NAM wind stress fields in these examples are recognizably similar in geographical patterns to the corresponding QuikSCAT wind stress fields in the middle two panels of the figure, there are large differences. Most obvious is the fact that the NAM wind stress fields are much smoother. The NAM stresses were only slightly weak in the 14 September 2003 example. In the 5 September 2004 example, however, the NAM stresses were much too weak. Locally intensified wind stress is found to the southwest of Cape Blanco and Cape Mendocino in both NAM examples. The offshore extent of these features in the 5 September 2004 example is more restricted than in the QuikSCAT wind fields. Moreover, the band of intensified wind stress off Cape Blanco in the 5 September 2004 example is considerably underestimated in the NAM Model.

The differences between the NAM and QuikSCAT wind stress fields become clearer in the derivative wind stress fields shown in the middle and right panels in Fig. 13. The NAM curl and divergence fields bear only vague resemblance to the QuikSCAT fields in Figs. 6c and 6d. In both examples, the small-scale features in the derivative wind stress fields from the model are weak and restricted to a region very near the coast. The spatial correlations of the NAM curl and divergence fields with the crosswind and downwind components of the RTG SST gradient field overlaid as contours in Fig. 13 are generally less than 0.3. A notable exception is that the correlations between the NAM divergence and downwind RTG SST gradient fields exceeded 0.6 during August–September 2004. The 5 September 2004 divergence field in Fig. 13 falls in the middle of this 2-month period of strong positive correlation. Note, however, the contradiction at about 40°N near Cape Mendocino where a band of divergence is associated with the wrong sign (negative) downwind SST gradient. This region coincides with the expansion fan downstream of Cape Mendocino.

Most of the structure in the model wind stress divergence fields in Fig. 13 can be associated with orographic effects. Couplets of convergence and divergence occur upstream and downstream, respectively, of every major promontory and bend in the coastline. Koračin and Dorman (2001) have previously noted this association from the fifth-generation Pennsylvania State University–National Center for Atmospheric Research Mesoscale Model (MM5). They attribute the convergence and divergence patterns to the hydraulic features (compression bulges and expansion fans) discussed in section 3 that develop in the marine atmospheric boundary layer because of bends in the coastline at the major capes. As in the NAM Model, these features in the MM5 model are restricted to the region very close to the coast.

The fundamental differences between the QuikSCAT and NAM summertime wind stress, curl, and divergence fields are summarized by the statistics in Fig. 14 computed from daily average fields. The standard deviation in all three characterizations of the wind stress field is underestimated in the NAM Model, both in magnitude and areal extent. The differences are especially profound in the curl and divergence fields; there is little variability in the summertime NAM curl and divergence fields except very near the coast. The model thus generates strong orographic effects in the immediate vicinities of major promontories, though not quantitatively accurate in detail (Perlin et al. 2004). It does a poor job, however, of representing the observed small-scale variability farther offshore that was shown in section 3 to be attributable to the influence of SST on the surface wind field.

It is noteworthy that the shortcomings of the NAM

[6] A thorough investigation of the NAM wind fields determined that the 10-m winds in the once-daily 0000 UTC analysis output files were inaccurate because of the details of how they are derived from the variables in the NAM Model. This problem did not affect the NAM forecast 10-m winds fields used in this study.

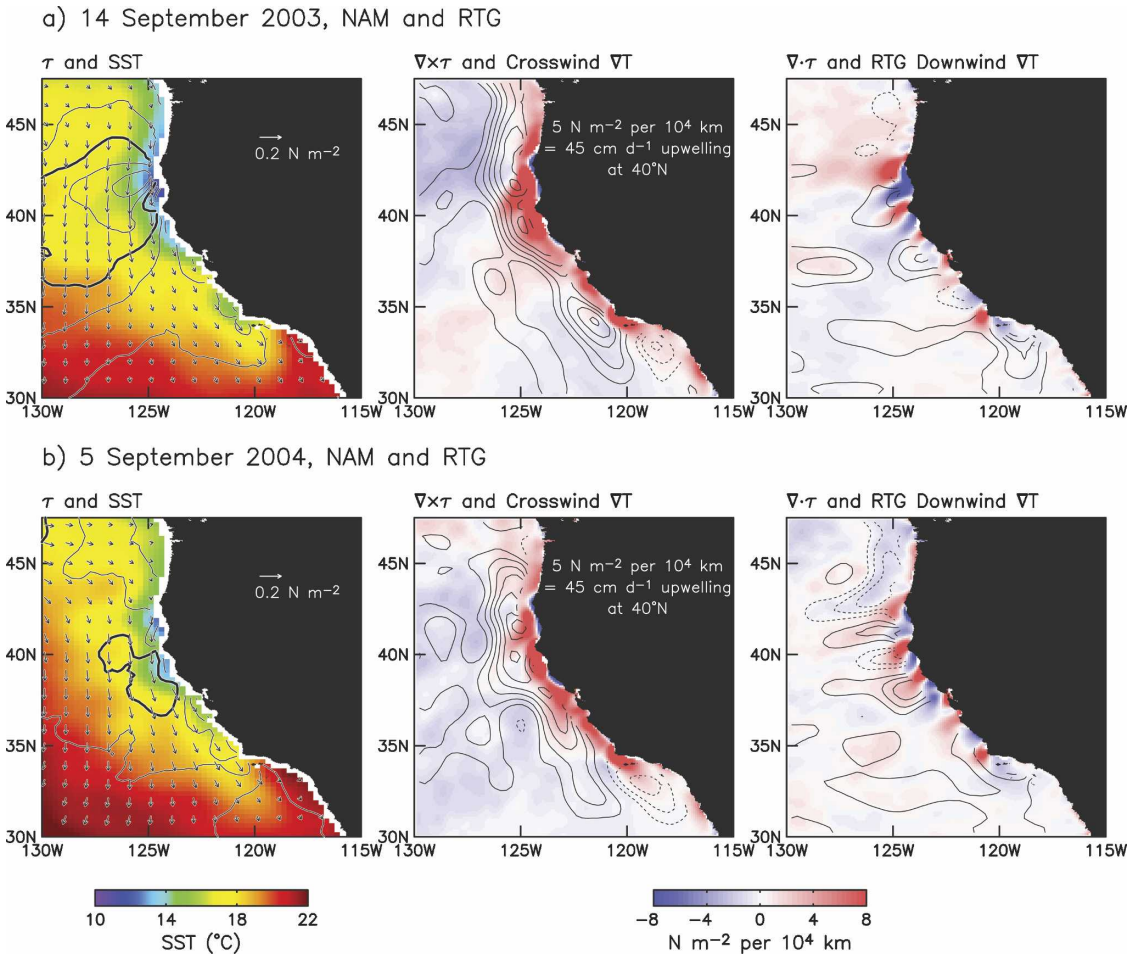

FIG. 13. As in Fig. 6 but for 29-day averages of the RTG SST fields and the NAM Model wind stress fields centered on (a) 14 Sep 2003 (the same time shown in Fig. 6c for QuikSCAT), and (b) 5 Sep 2004 (the same time shown in Fig. 6d for QuikSCAT).

Model wind fields are not apparent from correlations of the wind stresses with QuikSCAT observations. Perlin et al. found high vector correlations and complex correlations off the coast of Oregon. This is also evident in the left panel in Fig. 15 from the scalar correlations greater than 0.85 over most of the CCS domain between daily fields of the alongshore wind component in the NAM Model and QuikSCAT observations. The shortcomings in the NAM wind fields become apparent from correlations for the derivative wind stress fields (the curl and divergence, which are the dynamically important characteristics of the wind field for the ocean and lower atmosphere, respectively). Since spatial derivatives are effectively a spatial high-pass filtering operation, the wind stress curl and divergence fields highlight the small-scale variability that is poorly resolved in the NAM wind stress fields. Typical values of the correlations between the NAM and QuikSCAT wind stress curl fields are about 0.5 (middle panel in Fig. 15). There are regions over the inner CCS where the correlations are this high for the wind stress divergence, but the divergence correlations become very small beyond about 200 km from the coast (right panel).

The NAM Model has been shown to be sensitive to the resolution of the SST fields used as the surface boundary condition (Thiébaux et al. 2003). The importance of SST resolution has also been demonstrated for the MM5 mesoscale model (Chen et al. 2001) and for the coarser-resolution European Centre for Medium-Range Weather Forecasts (ECMWF) global forecast model (Chelton 2005; Chelton and Wentz 2005; Maloney and Chelton 2006). In view of the weak SST gradient magnitudes in the RTG SST analyses when compared with the AMSR-E observations (Figs. 13 and 14), it can be inferred that the inadequacies in the NAM summertime wind stress fields are due at least in part to

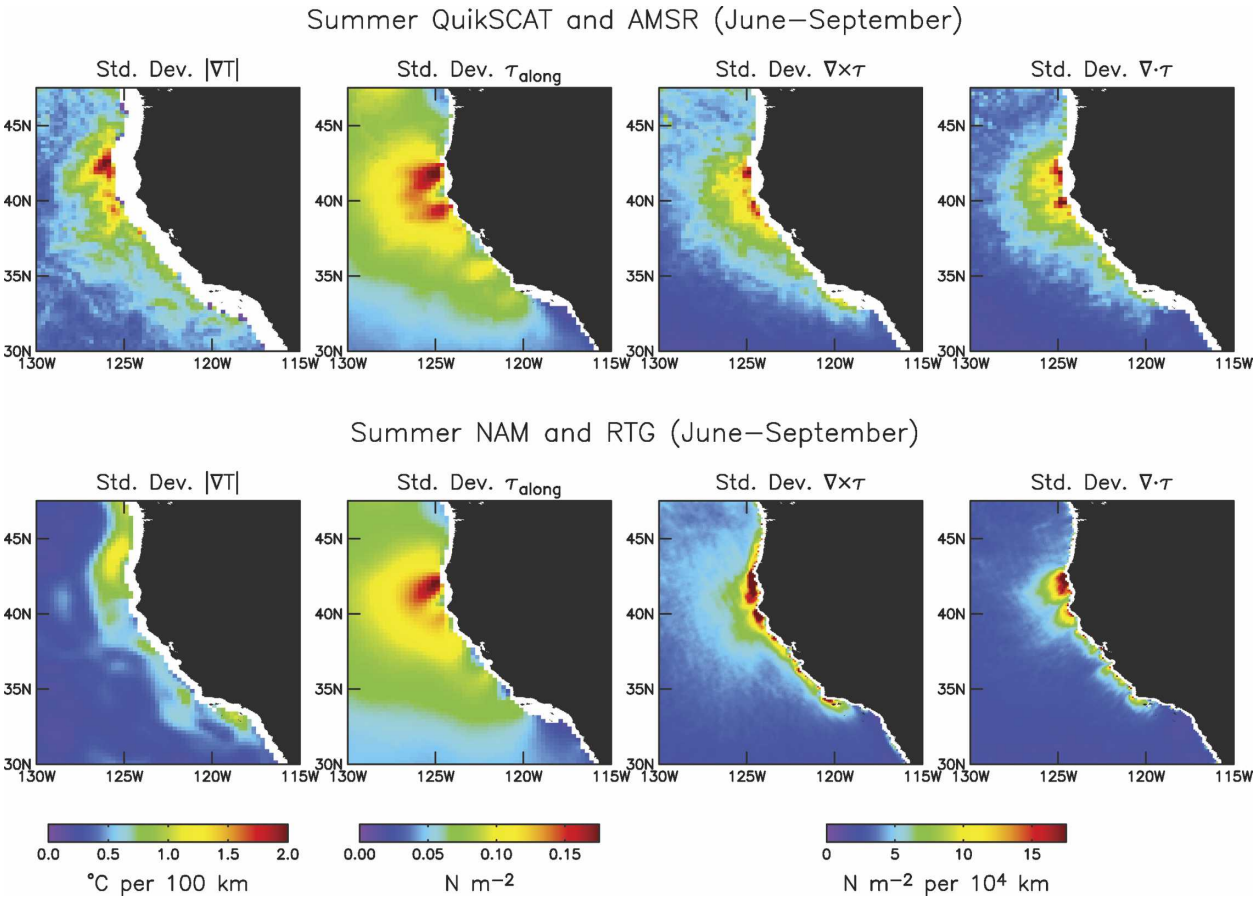

FIG. 14. Maps of summertime standard deviations of (left to right) the magnitude of the SST gradient, the alongshore wind stress, the wind stress curl, and the wind stress divergence. The top row corresponds to statistics computed from daily-averaged AMSR-E SST fields and QuikSCAT wind stress fields and the bottom row corresponds to statistics computed from daily-averaged RTG SST fields and NAM wind stress fields. The local alongshore direction at each 0.25° grid point was defined for both QuikSCAT and NAM based on the QuikSCAT wind stress variance ellipses as described in the caption for Fig. 10. All statistics were computed from the three summertime periods June–September during calendar years 2003–05.

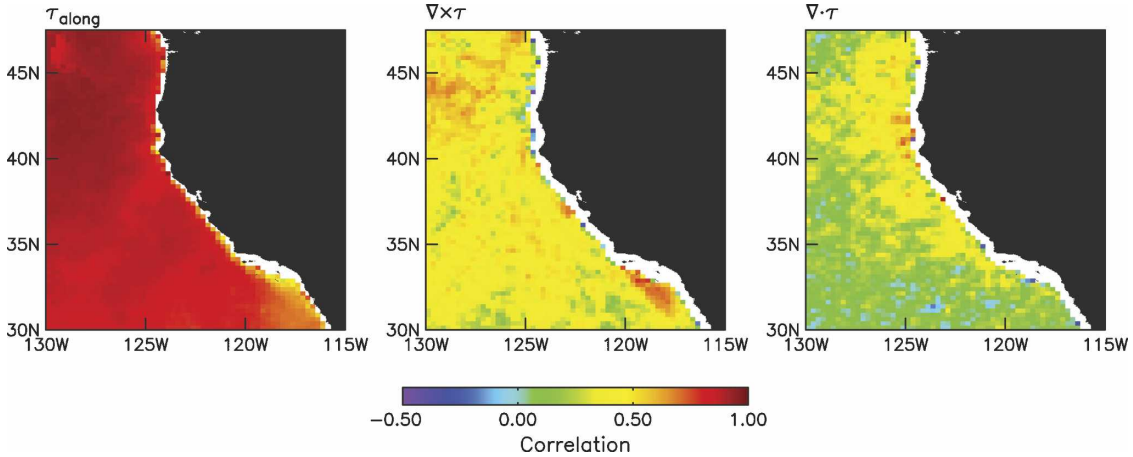

FIG. 15. Maps of the zero-lag cross-correlations between daily-average wind stress fields computed from QuikSCAT observations and the NAM Model in the three summertime periods June–September during calendar years 2003–05: (left) the alongshore component of wind stress, defined for both QuikSCAT and NAM based on the QuikSCAT wind stress variance ellipses as described in the caption for Fig. 10; (middle) the wind stress curl; and (right) the wind stress divergence.

inadequacies in the RTG SST fields used as the surface boundary condition in the NAM Model. The resolution of the RTG SST fields is poor in the CCS region because of the smoothing in the RTG objective analysis algorithm that is imposed to accommodate the sparse summertime AVHRR sampling owing to the frequent occurrence of stratus clouds over the CCS (see Figs. 1, 3, and 10 of Chelton and Wentz 2005). The observed SST-induced perturbations of the wind stress field will thus be poorly represented in the NAM Model, even if the influence of SST on the atmospheric boundary layer is accurately represented in the model. The problem may be exacerbated by the fact that most of the observations that are assimilated into the NAM Model are restricted to the very nearshore region (Figs. 1 and 2) and thus provide little information on the wind field farther offshore where SST influence on the surface wind field is so clearly evident in the satellite data.

Inadequacies in the parameterization of boundary layer processes may also contribute to the weak response of the NAM wind stress fields to spatial variability in the SST field. This has been shown to be the case in the coarser-resolution ECMWF global forecast model in the Tropics (Chelton 2005) and in midlatitudes (Maloney and Chelton 2006). The response of ECMWF wind stress fields to SST is about one-half as strong as the response inferred from QuikSCAT and AMSR-E data. Ongoing studies suggest that this is because boundary layer mixing is too strong in the ECMWF model (A. Beljaars 2005, personal communication). Since the heritage of the mixing parameterizations in the mesoscale models is the global forecast models, it is possible that similar problems exist in the mesoscale models and contribute to the inadequacies in the SST influence on the wind stress fields in these models.

The structures of the NAM wind stress fields appear to be very similar to those in the MM5 mesoscale atmospheric model. Koračin et al. (2004) found that the curl fields in the MM5 are characterized by small areas of very strong positive curl that hug the coastline in the lee of every major promontory and sharp bend along the California and Oregon coasts. Koračin and Dorman (2001) found that patches of wind divergence in the MM5 are similarly restricted to the very nearshore region near major promontories. It can be concluded that the wind fields in the NAM and MM5 mesoscale atmospheric models do a poor job of representing SST-induced variability over the CCS in the region beyond about 50 km from the coast that is resolved in the QuikSCAT wind stress curl and divergence fields analyzed in this study.

In contrast to the NAM Model and MM5, the recent study by Haack et al. (2005) showed that the U.S. Navy Coupled Ocean–Atmospheric Mesoscale Prediction System (COAMPS) model run in a noncoupled configuration is capable of generating well-defined SST influence on the wind stress curl field. Small-scale features in the curl field in the offshore region were shown to be related to crosswind SST gradients associated with meandering SST fronts in the CCS. Identifying the reason for the apparent improved representation of the small-scale structure in the wind stress curl field offshore in the COAMPS model is beyond the scope of this study. The most likely explanation is that the optimally interpolated SST analyses used as the surface boundary condition (Cummings 2003) have a higher resolution than the RTG SST fields used for the NAM Model and MM5. While the quantitative accuracy of the COAMPS model is not yet known, the significantly better representation of small-scale variability in the winds stress fields reported by Haack et al. (2005) is very encouraging. The QuikSCAT data presented in this study can be used to assess the accuracy of the COAMPS model simulations.

6. Discussion

A crucial precursor to the onset of summertime conditions favorable to SST influence on surface wind stress in the CCS is the establishment of a SST front associated with the separation of the summertime equatorward coastal jet that occurs at Cape Blanco (Barth and Smith 1998; Barth et al. 2000, 2005), or possibly about 100 km to the north at Heceta Bank (Castelao et al. 2005). This SST front spreads offshore and downstream (equatorward) as a meandering jet. The mechanism for the jet separation from the Oregon coast is not fully understood but it has been speculated that both coastal upwelling and Ekman upwelling from nearshore wind stress curl play important roles (Samelson et al. 2002; Castelao and Barth 2007). The offshore migration of the SST front establishes a spatially varying SST field that causes the wind stress to decrease over cold water and increase over warm water. This generates patchiness of the wind stress curl field and associated Ekman upwelling or downwelling in regions where the winds blow parallel to isotherms (perpendicular to the SST gradient vector). Likewise, wind stress divergence or convergence develop where the winds blow across isotherms. These small-scale structures in the curl and divergence fields evolve over the course of the summertime upwelling season as the structures of the SST fronts evolve.

The dynamical importance of the summertime SST-induced perturbations of the wind stress field can be assessed from simple statistics of the wind stress curl

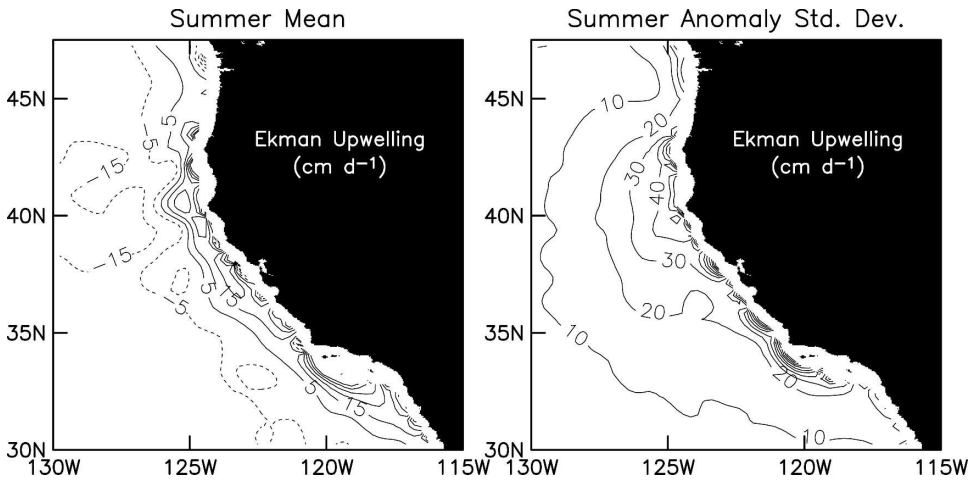

FIG. 16. Statistics of summertime 29-day-average Ekman upwelling velocity computed from wind stress curl fields derived from the six summertime periods June–September of QuikSCAT data during calendar years 1999–2005. (left) The overall average summertime Ekman upwelling velocity field with a contour interval of 10 cm day^{-1} (negative contours are shown as dashed lines). (right) The standard deviation of the anomaly Ekman upwelling velocity (computed from the deviations of each of the summertime 29-day-average fields from the overall 6-yr summertime average at left), with a contour interval of 10 cm day^{-1}.

fields. The overall average summertime (June–September) Ekman upwelling velocity field associated with the wind stress curl averaged over six years of QuikSCAT data (August 1999–September 2005) is shown in the left panel in Fig. 16. Summertime anomaly wind stress curl fields were computed as the deviation of each 29-day-average summertime wind stress curl field from the overall average. From the standard deviation of the associated summertime anomaly Ekman upwelling velocity fields (right panel in Fig. 16), the typical deviations from the overall mean are seen to be larger than the mean value everywhere except very near the coast. Since the spatial variability of the wind stress curl field on the monthly time scales considered in this study is largely determined by the SST field (see the middle panels in Fig. 6), it can be inferred that the SST effects are $O(1)$ perturbations of the mean Ekman upwelling conditions.

From the distributions of the mean versus anomaly summertime Ekman upwelling velocities in Fig. 17, it is evident that the dynamic range of the anomalies is larger than that of the mean. Only 8% of the mean Ekman upwelling velocities exceeded 20 cm day^{-1}. The 29-day-average anomaly Ekman upwelling velocities had a root-mean-square value of 18.6 cm day^{-1} and 18% of the 29-day average anomalies (positive and negative) were larger in magnitude than 20 cm day^{-1}. The feedback effects of these energetic SST-induced perturbations of the Ekman upwelling velocity on the ocean are undoubtedly important to the ocean circulation and likely modify the SST field. In comparison, Marchesiello et al. (2003, see their Fig. 8) found that terms in their model mean CCS vorticity balance (which included the wind stress curl) are on the order of 1 N m^{-2} (10^4 km)$^{-1}$, an order of magnitude smaller

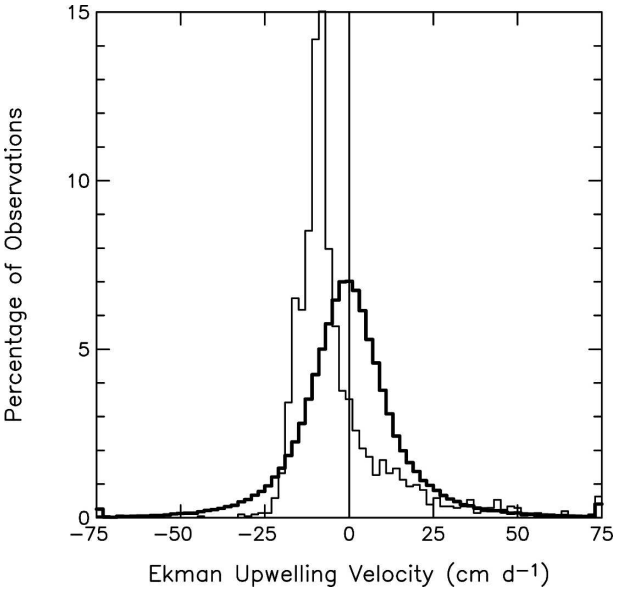

FIG. 17. Histograms of summertime Ekman upwelling velocities computed from 29-day-average QuikSCAT wind stress curl fields during the six summertime periods June–September during calendar years 1999–2005. The thin line corresponds to the distribution of the overall 6-yr-average summertime Ekman upwelling velocity field in the left panel of Fig. 16. The thick line corresponds to the summertime anomaly Ekman upwelling velocity fields from which the standard deviation map in the right panel of Fig. 16 was constructed.

than the observed 29-day-average SST-induced perturbations of the wind stress curl field in the QuikSCAT observations (see Fig. 14).

In view of the large magnitudes of the SST-induced perturbations of the Ekman upwelling velocity field, the atmosphere and ocean off the U.S. West Coast must be considered a fully coupled system. The SST-induced perturbations of the wind stress field may also have biological importance since Ekman upwelling brings nutrient-rich deep water to the upper ocean where primary production occurs.

An unfortunate limitation of the satellite data analyzed here is that it is only possible to determine the SST influence on wind field beyond about 100 km from the coast. This limitation is imposed by the inability to determine SST gradients closer than about 100 km from land from AMSR-E data. The strong influence of SST on the wind field found here in the offshore region surely is important in the inshore region as well. However, it is likely that orographic effects become progressively more important in the inshore regions, complicating the structures in the wind stress curl and divergence fields.

The observations recently reported by Koračin et al. (2005) may be evidence of SST influence on the surface winds very near the coast. They found that measured wind stress curl in the very nearshore region is negatively correlated with SST, which they interpret as an indication that the cold water very near the coast is generated by the wind stress curl rather than by coastal upwelling from the alongshore wind stress at the coast. An alternative interpretation based on the results obtained in this study in the offshore region is that the cold water from coastal upwelling may modify the nearshore wind stress field in a manner that results in positive wind stress curl due to stabilization of the atmospheric boundary layer and an associated decrease in the alongshore wind stress toward the coast where the water is coldest. Warming of the water very near the coast, either from reduced coastal upwelling or from remote forcing in the form of poleward-propagating coastally trapped waves, would reduce the nearshore wind stress curl, thus resulting in a negative correlation between SST and wind stress curl like that reported by Koračin et al. (2005). Bane et al. (2005) and Samelson et al. (2002) present evidence for formation of stable internal boundary layers over cold upwelled water along the Oregon coast that are consistent with this interpretation.

7. Conclusions

Satellite measurements of wind stress by QuikSCAT and of SST by the AMSR-E were analyzed to investigate the influence of SST on the surface wind stress field in the CCS. This analysis adds to a growing list of studies showing the importance of ocean–atmosphere interaction in regions of strong SST fronts (see the reviews by Xie 2004 and Chelton et al. 2004). The scales of this coupling are smaller in the CCS than in most regions analyzed in previous studies. During the summertime when SST fronts are well developed in the CCS, the effects of air–sea heat fluxes on stability and mixing in the lower atmosphere increase the wind stress over warm water and decrease it over cold water. Spatial variability of this SST influence in the vicinity of SST fronts generates wind stress curl and divergence that are linearly related to, respectively, the crosswind and downwind components of the SST gradient field. This ocean–atmosphere interaction is not clearly evident in the CCS region during the wintertime because SST gradients are weak and disorganized and the wind direction is highly variable.

The observed strong influence of SST on the wind stress field was shown to be poorly represented in the NAM Model. The MM5 appears to have deficiencies similar to those of the NAM Model. In contrast, the COAMPS model output recently analyzed by Haack et al. (2005) produces SST-induced small-scale structures in the wind stress curl field that are much more realistic than in the NAM Model and MM5. It was suggested in section 5 that this is likely attributable to improved resolution of the SST boundary condition used in the COAMPS model.

Wind stress fields from the NAM, MM5, and COAMPS are being used to force ocean models of the CCS. Forcing the ocean models with more accurate QuikSCAT-based wind stress fields is tempting, but the likely two-way coupling between SST and wind stress poses a potential problem with this solution to inadequacies in the mesoscale atmospheric models. The SST-induced wind stress curl perturbations feed back on the ocean and cause the SST field to evolve in a specific manner in the real ocean, perhaps acting to sustain the SST structures or to cause them to migrate offshore. Unless the ocean model produces a SST field that is quantitatively compatible with the QuikSCAT observed wind stress field, such coupling between the wind stress and the SST field will be misrepresented in the QuikSCAT-forced ocean model. This could produce undesirable features in the ocean model simulation.

The better approach is to simulate the CCS with a fully coupled ocean–atmosphere model. Significant progress has recently been made in coupled modeling of the CCS. Seo et al. (2007) modeled the CCS with the Scripps Coupled Ocean–Atmosphere Regional

(SCOAR) model with horizontal resolutions of 7 km for the ocean component of the model and 16 km for the atmosphere component. In the configuration used for their study, large-scale forcing of the SCOAR model was provided by the National Centers for Environmental Prediction (NCEP) reanalysis fields but the model did not include any data assimilation components. Although weaker than in the satellite observations in Fig. 7, the model produced realistic SST-induced structures in the wind stress curl and divergence fields that are linearly related to the model crosswind and downwind SST gradients, respectively, as expected from Fig. 7. Analysis is under way to investigate the feedback effects of SST-induced perturbations of the wind stress curl field on the ocean circulation in the SCOAR model.

As a closing remark, we note that the SST gradients in the AMSR-E data analyzed here are lower-bound estimates because of the coarse 56-km footprint size of the measurements. Higher-resolution measurements are desirable for this analysis but summertime stratus clouds often obscure much of the CCS in high-resolution infrared measurements by the AVHRR on the polar-orbiting NOAA satellites. Newly available infrared measurements of SST from the *Geostationary Operational Environmental Satellite* (*GOES-10*) extending back in time to June 2000 offer promising prospects for high-resolution SST fields in the CCS. The advantage of *GOES-10* data over the AVHRR data are that measurements of a given location on the sea surface can be obtained every 30 minutes, thus increasing the likelihood of observing clear-sky conditions when compared with the 2-times-per-day sampling of a polar-orbiting satellite. Four years of these SST gradient fields have recently been analyzed by Castelao et al. (2005, 2006) to study the separation of the coastal jet from the Oregon coast and the seasonal cycle of SST frontal variability throughout the CCS. With the present processing algorithms, these data have a resolution of 5 km and can provide SST gradient fields to within about 15–20 km of land. Efforts are under way to determine whether monthly resolution of the SST gradient field can be obtained from *GOES-10* data. Such data would greatly enhance the present study of the SST influence on surface wind stress, especially in conjunction with the 12.5-km QuikSCAT wind stress fields with a smaller data gap near land that are presently under development.

Acknowledgments. The wind stress field over the CCS has been a subject of interest to the lead author of this paper for more than 25 years since working for three years at the Jet Propulsion Laboratory beginning in 1980 with the specific goal of investigating the wind field in the CCS region from analysis of the scatterometer data that would "soon be available" from the NASA Scatterometer (NSCAT) mission. NSCAT eventually launched 17 years later in August 1996, but the data record ended prematurely after only 9 months of operation because of a failure of the solar array panel. QuikSCAT was launched two years later as a "quick recovery mission." On the 19 June 2006 date of the final revision of this manuscript, QuikSCAT celebrated the seventh anniversary of its launch. The long wait for the simultaneous satellite observations of wind stress and SST that were necessary for this analysis has finally been rewarded. We thank Mike Freilich for his tireless efforts over two decades as Project Scientist for NSCAT and Mission Principal Investigator for the SeaWinds scatterometers on the QuikSCAT and *ADEOS-II* satellites. If not for his tenacity and dedication to scatterometry, QuikSCAT data would still not be available. We also thank Frank Wentz at Remote Sensing Systems for developing the geophysical retrieval algorithm for the AMSR-E SST fields that were also crucial to the analysis presented here.

The NAM wind fields used in this study were acquired from NOAA and provided by Phil Barbour at OSU. We thank Brian Zelenke at OSU for extracting the 0300 and 1500 UTC NAM forecast fields and converting them into an easily readable format. Phil Barbour helped to identify the problem with the 10-m wind analyses noted in footnote 6 in section 5. Renato Castelao, Ed Dever, Clive Dorman, Tracy Haack, Jane Huyer, Darko Koračin, Natalie Perlin, Julie Pullen, Bob Smith, Ted Strub, and two anonymous reviewers provided valuable comments on the manuscript. This research was supported by NASA Grant NAS5-32965 and Contracts 1283973 and 1283976 from the NASA Jet Propulsion Laboratory for funding of Ocean Vector Winds Science Team activities, NSF Grant OCE-0218812, and Award NA03NES4400001 to Oregon State University from the National Oceanic and Atmospheric Administration (NOAA), U.S. Department of Commerce. The statements, findings, conclusions, and recommendations are those of the authors and do not necessarily reflect the views of NOAA or the Department of Commerce.

REFERENCES

Bane, J. M., M. D. Levine, R. M. Samelson, S. M. Haines, M. F. Meaux, N. Perlin, P. M. Kosro, and T. Boyd, 2005: Atmospheric forcing of the Oregon coastal ocean during the 2001 upwelling season. *J. Geophys. Res.,* **110,** C10S02, doi:10.1029/2004JC002653.

Barth, J. A., and R. L. Smith, 1998: Separation of a coastal up-

welling jet at Cape Blanco, Oregon, USA. *S. Afr. J. Mar. Sci.,* **19,** 5–14.

——, S. D. Pierce, and R. L. Smith, 2000: A separating coastal upwelling jet at Cape Blanco, Oregon and its connection to the California Current System. *Deep-Sea Res. II,* **47,** 783–810.

——, ——, and T. J. Cowles, 2005: Mesoscale structure and its seasonal evolution in the northern California Current System. *Deep-Sea Res. II,* **52,** 5–28.

Burk, S., and W. Thompson, 1996: The summertime low-level jet and marine boundary layer structure along the California coast. *Mon. Wea. Rev.,* **124,** 668–686.

——, T. Haack, and R. M. Samelson, 1999: Mesoscale simulation of supercritical, subcritical, and transcritical flow along coastal topography. *J. Atmos. Sci.,* **56,** 2780–2795.

Castelao, R. M., and J. A. Barth, 2007: The role of wind-stress curl in jet separation at a cape. *J. Phys. Oceanogr.,* in press.

——, ——, and T. P. Mavor, 2005: Flow–topography interactions in the northern California Current System observed from geostationary satellite data. *Geophys. Res. Lett.,* **32,** L24612, doi:10.1029/2005GL024401.

——, T. P. Mavor, J. A. Barth, and L. C. Breaker, 2006: Sea surface temperature fronts in the California Current System from geostationary satellite observations. *J. Geophys. Res.,* **111,** C09026, doi:10.1029/2006JC003541.

Chelton, D. B., 2005: The impact of SST specification on ECMWF surface wind stress fields in the eastern tropical Pacific. *J. Climate,* **18,** 530–550.

——, and M. G. Schlax, 2003: The accuracies of smoothed sea surface height fields constructed from tandem satellite altimeter datasets. *J. Atmos. Oceanic Technol.,* **20,** 1276–1302.

——, and M. H. Freilich, 2005: Scatterometer-based assessment of 10-m wind analyses from the operational ECMWF and NCEP numerical weather prediction models. *Mon. Wea. Rev.,* **133,** 409–429.

——, and F. J. Wentz, 2005: Global microwave satellite observations of sea surface temperature for numerical weather prediction and climate research. *Bull. Amer. Meteor. Soc.,* **86,** 1097–1115.

——, and Coauthors, 2001: Observations of coupling between surface wind stress and sea surface temperature in the eastern tropical Pacific. *J. Climate,* **14,** 1479–1498.

——, M. G. Schlax, M. H. Freilich, and R. F. Milliff, 2004: Satellite measurements reveal persistent small-scale features in ocean winds. *Science,* **303,** 978–983.

Chen, S. S., W. Zhao, J. E. Tenerelli, R. H. Evans, and V. Halliwell, 2001: Impact of AVHRR sea surface temperature on atmospheric forcing in the Japan/East Sea. *Geophys. Res. Lett.,* **28,** 4539–4542.

Cummings, J. A., 2003: Ocean data assimilation. COAMPS: Version 3 model description, NRL Publ. NRL/PU/7500-03-448, NRL, 21–28. [Available from the Naval Research Laboratory, Monterey, CA 93943-5502.]

Cushman-Roisin, B., 1994: *Introduction to Geophysical Fluid Dynamics*. Prentice Hall, 320 pp.

de Szoeke, S. P., and C. S. Bretherton, 2004: Quasi-Lagrangian large eddy simulations of cross-equatorial flow in the east Pacific atmospheric boundary layer. *J. Atmos. Sci.,* **61,** 1837–1858.

Dever, E. P., C. E. Dorman, and J. L. Largier, 2006: Surface boundary layer variability off northern California, USA during upwelling. *Deep-Sea Res. II,* **53,** 2887–2905.

Dorman, C. E., 1985: Hydraulic control of the northern California marine layer (abstract). *Eos, Trans. Amer. Geophys. Union,* **66,** 914.

——, D. P. Rogers, W. Nuss, and W. T. Thompson, 1999: Adjustment of the summer marine boundary layer around Pt. Sur, California. *Mon. Wea. Rev.,* **127,** 2143–2159.

——, T. Holt, D. P. Rogers, and K. A. Edwards, 2000: Large-scale structure of the summertime marine boundary layer along Oregon and California. *Mon. Wea. Rev.,* **128,** 1632–1652.

Edwards, K. A., A. M. Rogerson, C. D. Winant, and D. P. Rogers, 2001: Adjustment of the marine atmospheric boundary layer to a coastal cape. *J. Atmos. Sci.,* **58,** 1511–1528.

——, D. P. Rogers, and C. E. Dorman, 2002: Adjustment of the marine atmospheric boundary layer to the large-scale bend in the California coast. *J. Geophys. Res.,* **107,** 3213, doi:10.1029/2001JC000807.

Enriquez, A. G., and C. A. Friehe, 1995: Effects of wind stress and wind stress curl variability on coastal upwelling. *J. Phys. Oceanogr.,* **25,** 1651–1671.

Freilich, M. H., and R. S. Dunbar, 1999: The accuracy of the NSCAT-1 vector winds: Comparisons with National Data Buoy Center buoys. *J. Geophys. Res.,* **104,** 11 231–11 246.

Gill, A. E., 1982: *Atmosphere–Ocean Dynamics*. Academic Press, 662 pp.

Haack, T., S. D. Burk, C. Dorman, and D. Rogers, 2001: Supercritical flow interaction within the Cape Blanco–Cape Mendocino orographic complex. *Mon. Wea. Rev.,* **129,** 688–708.

——, ——, and R. M. Hodur, 2005: U.S. west coast surface heat fluxes, wind stress, and wind stress curl from a mesoscale model. *Mon. Wea. Rev.,* **133,** 3202–3216.

Huddleston, J. N., and B. W. Stiles, 2000: Multidimensional histogram (MUDH) rain flag product description (version 3.0). Jet Propulsion Laboratory, Pasadena, CA, 8 pp. [Available online at ftp://podaac.jpl.nasa.gov/pub/ocean_wind/quikscat/L2B/doc/MUDH_Description_V3.pdf.]

Huyer, A. E., E. J. Sobey, and R. L. Smith, 1979: The spring transition in currents over the Oregon continental shelf. *J. Geophys. Res.,* **84,** 6995–7011.

——, J. H. Fleischbein, J. Keister, P. M. Kosro, N. Perlin, R. L. Smith, and P. A. Wheeler, 2005: Two coastal upwelling domains in the northern California Current system. *J. Mar. Res.,* **63,** 901–929.

Jury, M. R., and N. Walker, 1988: Marine boundary layer modification across the edge of the Agulhas Current. *J. Geophys. Res.,* **93,** 647–654.

Koračin, D., and C. E. Dorman, 2001: Marine atmospheric boundary layer divergence and clouds along California in June 1996. *Mon. Wea. Rev.,* **129,** 2040–2055.

——, ——, and E. P. Dever, 2004: Coastal perturbations of marine layer winds, wind stress, and wind stress curl along California and Baja California in June 1999. *J. Phys. Oceanogr.,* **34,** 1152–1173.

——, A. Kochanski, C. E. Dorman, and E. P. Dever, 2005: Wind stress curl and upwelling along the California coast. *Bull. Amer. Meteor. Soc.,* **86,** 629–630.

Large, W. G., J. C. McWilliams, and S. C. Doney, 1994: Oceanic vertical mixing: A review and a model with a nonlocal boundary layer parameterization. *Rev. Geophys.,* **32,** 363–403.

Maloney, E. D., and D. B. Chelton, 2006: An assessment of the sea surface temperature influence on surface wind stress in numerical weather prediction and climate models. *J. Climate,* **19,** 2743–2762.

Marchesiello, P., J. McWilliams, and A. Shchepetkin, 2003: Equi-

librium structure and dynamics of the California Current System. *J. Phys. Oceanogr.,* **33,** 753–783.

Mears, C. A., D. K. Smith, and F. J. Wentz, 2001: Comparison of Special Sensor Microwave Imager and buoy-measured wind speeds from 1987 to 1997. *J. Geophys. Res.,* **106,** 11 719–11 729.

O'Neill, L. W., D. B. Chelton, and S. K. Esbensen, 2003: Observations of SST-induced perturbations of the wind stress field over the Southern Ocean on seasonal time scales. *J. Climate,* **16,** 2340–2354.

——, ——, ——, and F. J. Wentz, 2005: High-resolution satellite observations of SST modification of the marine atmospheric boundary layer over the Agulhas Return Current. *J. Climate,* **18,** 2706–2723.

Perlin, N., R. M. Samelson, and D. B. Chelton, 2004: Scatterometer and model wind and wind stress in the Oregon–Northern California coastal zone. *Mon. Wea. Rev.,* **132,** 2110–2129.

Pickett, M. H., and J. D. Paduan, 2003: Ekman transport and pumping in the California Current based on the U.S. Navy's high-resolution atmospheric model (COAMPS). *J. Geophys. Res.,* **108,** 3327, doi:10.1029/2003JC001902.

——, W. Tang, L. K. Rosenfeld, and C. H. Wash, 2003: QuikSCAT satellite comparisons with nearshore buoy wind data off the U.S. west coast. *J. Atmos. Oceanic Technol.,* **20,** 1869–1879.

Rogers, E., T. Black, B. Ferrier, Y. Lin, D. Parrish, and G. DiMego, 2001: Changes to the NCEP Meso Eta Analysis and Forecast System: Increase in resolution, new cloud microphysics, modified precipitation assimilation, and modified 3DVAR analysis. NWS Tech. Procedures Bulletin, 488, 15 pp. [Available online at http://wwwt.emc.ncep.noaa.gov/mmb/mmbpll/eta12tpb/ or from the National Weather Service, Office of Meteorology, 1325 East-West Highway, Silver Spring, MD 20910.]

——, and Coauthors, 2005: The NCEP North American Mesoscale Modeling System: Final Eta model/analysis changes and preliminary experiments using the WRF-NMM. Preprints, *21st Conf. on Weather Analysis and Forecasting/17th Conf. on Numerical Weather Prediction,* Washington, DC, Amer. Meteor. Soc., CD-ROM, 4B.5.

Rogerson, A. M., 1999: Transcritical flows in the coastal marine atmospheric boundary layer. *J. Atmos. Sci.,* **56,** 2761–2779.

Samelson, R. M., 1992: Supercritical marine-layer flow along a smoothly varying coastline. *J. Atmos. Sci.,* **49,** 1571–1584.

——, and S. J. Lentz, 1994: The horizontal momentum balance in the marine atmospheric boundary layer during CODE-2. *J. Atmos. Sci.,* **51,** 3745–3757.

——, and Coauthors, 2002: Wind stress forcing of the Oregon coastal ocean during the 1999 upwelling season. *J. Geophys. Res.,* **107,** 3034, doi:10.1029/2001JC000900.

——, E. D. Skyllingstad, D. B. Chelton, S. K. Esbensen, L. W. O'Neill, and N. Thum, 2006: On the coupling of wind stress and sea surface temperature. *J. Climate,* **19,** 1557–1566.

Schlax, M. G., D. B. Chelton, and M. H. Freilich, 2001: Sampling errors in wind fields constructed from single and tandem scatterometer datasets. *J. Atmos. Oceanic Technol.,* **18,** 1014–1036.

Seo, H., A. J. Miller, and J. O. Roads, 2007: The Scripps Coupled Ocean–Atmosphere Regional (SCOAR) model, with applications in the eastern Pacific sector. *J. Climate,* **20,** 381–402.

Small, R. J., S.-P. Xie, Y. Wang, S. K. Esbensen, and D. Vickers, 2005: Numerical simulation of boundary layer structure and cross-equatorial flow in the eastern Pacific. *J. Atmos. Sci.,* **62,** 1812–1830.

Stiles, B. W., and S. H. Yueh, 2002: Sea surface winds—Impact of rain on spaceborne Ku-band wind scatterometer data. *IEEE Trans. Geosci. Remote Sens.,* **40,** 1973–1983.

Stoffelen, A., 1998: Toward the true near-surface wind speed: Error modeling and calibration using triple collocation. *J. Geophys. Res.,* **103,** 7755–7766.

Strub, P. T., and C. James, 1988: Atmospheric conditions during the spring and fall transitions in the coastal ocean off the western United States. *J. Geophys. Res.,* **93,** 15 561–15 584.

——, and ——, 2000: Altimeter-derived variability of surface velocities in the California Current System: 2. Seasonal circulation and eddy statistics. *Deep-Sea Res. II,* **47,** 831–870.

Sweet, W. R., R. Fett, J. Kerling, and P. La Violette, 1981: Air–sea interaction effects in the lower troposphere across the north wall of the Gulf Stream. *Mon. Wea. Rev.,* **109,** 1042–1052.

Thiébaux, J., E. Rogers, W. Wang, and B. Katz, 2003: A new high-resolution blended real-time global sea surface temperature analysis. *Bull. Amer. Meteor. Soc.,* **84,** 645–656.

Wallace, J. M., T. P. Mitchell, and C. Deser, 1989: The influence of sea surface temperature on surface wind in the eastern equatorial Pacific: Seasonal and interannual variability. *J. Climate,* **2,** 1492–1499.

Winant, C. D., C. E. Dorman, C. A. Friehe, and R. C. Beardsley, 1988: The marine layer off Northern California: An example of supercritical channel flow. *J. Atmos. Sci.,* **45,** 3588–3605.

Woodruff, S. D., R. J. Slutz, R. J. Jenne, and P. M. Steurer, 1987: A comprehensive ocean–atmosphere data set. *Bull. Amer. Meteor. Soc.,* **68,** 1239–1250.

Xie, S.-P., 2004: Satellite observations of cool ocean–atmosphere interaction. *Bull. Amer. Meteor. Soc.,* **85,** 195–208.